Intercomparison of optical scattering turbidity sensors for a wide range of suspended sediment types and concentrations

Maarten Bakker, Cédric Legout, Romain Biron, Guillaume Nord, Caroline Le Bouteiller, Laurie Boithias, B. Camenen, Solenn Cotel, Catherine Coulaud, Hervé Denis, et al.

Intercomparison of optical scattering turbidity sensors for a wide range of suspended sediment types and concentrations

Maarten Bakker[1], Cédric Legout[1], Romain Biron[1], Guillaume Nord[1], Caroline Le Bouteiller[1], Laurie Boithias[2], Benoît Camenen[3], Solenn Cotel[4], Catherine Coulaud[1], Hervé Denis[1], Guillaume Dramais[3], Jessica Droujko[5], Ophélie Fovet[6], Guilhem Freche[1], Manuela Grippa[2], Jérôme Le Coz[3], Antoine Lucas[7], Jean-Michel Martinez[2], François Meric[6], Henri Mora[1], Julien Némery[1], Dahédrey Payandi-Rolland[8], Gilles Pierrefeu[9], Anne Probst[8], Jean-Luc Probst[8], Damien Raclot[10], Olivier Ribolzi[2], Christophe Rousseau[1], Sébastien Salvador-Blanes[11], William Santini[2], Fabien Seve[1], Fabien Thollet[3], Pierre Vanhooydonck[11], Sébastien Zanker[12]

Corresponding author: Maarten Bakker (maartenbakker@yahoo.com)

[1]University Grenoble Alpes, IGE (Institute for Geosciences and Environmental Research), CNRS, INRAE, IRD, Grenoble INP, Grenoble, France
[2]University of Toulouse III, GET (Environmental Geosciences Toulouse), CNRS, IRD, CNES, Toulouse, France
[3]INRAE (National Research Institute for Agriculture, Food and Environment), RiverLy, Villeurbanne, France
[4]University of Strasbourg, LHyGeS (Laboratory of Hydrology and Geochemistry), CNRS, ENGEES, Strasbourg, France
[5]ETH Zürich, Institute of Environmental Engineering, Zürich, Switzerland
[6]INRAE (National Research Institute for Agriculture, Food and Environment), Institut Agro, SAS, Rennes, France
[7]University of Paris, IPGP (Institut de Physique du Globe de Paris), Paris, France
[8]University of Toulouse, Ecolab (Laboratory of Functional Ecology and Environment), CNRS, Castanet-Tolosan, France
[9]CNR, CACOH (Hydraulic Structure Behaviour Analysis Centre), Lyon, France
[10]University of Montpellier, LISAH (Soil-Agrosystem-Hydrosystem Interaction), INRAE, IRD, Institut Agro, Montpellier, France
[11]University of Tours, GéHCO (Continental Geohydrosystems), Tours, France
[12]Électricité de France, DTG division, Grenoble, France

ABSTRACT

In order to monitor the effects of rapid changes in climate and land use on sediment export from erodible environments, it is crucial to accurately quantify highly-fluctuating suspended-sediment concentrations (SSCs) in river systems that drain small to meso-scale catchments. We performed laboratory experiments to study optical scattering measurements from 7 different types of turbidity sensors and sediment from 12 sources to quantify SSCs in the range of 0.05–100 g/L. We find that measurements of scattered light from multiple angles may allow for: (1) an extended monitoring range with SSCs up to 10–100 g/L, where enhanced uncertainty may occur near the transition in the effective operational ranges of the underlying signals (typically somewhere in the range of 1–10 g/L); and/or (2) a slightly reduced sensitivity to source-dependent sediment properties. The specific turbidity of the investigated sensors is inversely related to particle diameter (D_{10}) for SSCs up to 1–5 g/L. Backscatter and combined-signal sensors also show a dependency on sediment colour (CIE a^*), which becomes particularly prominent at SSCs above 10 g/L. We relate this increase in colour dependency with SSC to the cumulative effect of near-infrared light absorption associated with multiple scattering. We discuss covarying physical properties of naturally-occurring river sediment that can dampen or enhance measurement sensitivity and result in turbidity-based SSC rating curves that may strongly differ in magnitude and form from curves derived for industrially-prepared material that is often used for sensor calibration. Although we generally find less than one order-of-magnitude differences in SSC per sensor among the sediment sources, systematic errors and uncertainties may disproportionally affect the quantification of fluvial sediment loads. This is particularly the case for high SSCs during large-magnitude flow events, which contribute strongly to total sediment export and are expected to become more prominent with ongoing climate change.

KEYWORDS

nephelometry, backscattering, turbidity ratio, multiple scattering, particle size, sediment colour, mountainous and Mediterranean environments

HIGHLIGHTS

- We tested 7 types of turbidity sensors for concentrations in the range 0.05–100 g/L
- Measurements per sensor varied within a factor of 10 among sediment from 12 sources
- Complementary scattering signals may allow for an extended SSC monitoring range,
- and/or reduced sensitivity to covarying physical properties of river sediment
- Sensors are increasingly sensitive to sediment colour for concentrations >10 g/L

1. INTRODUCTION

Ongoing human-induced changes in the landscape and climate have a profound impact on sediment loads in rivers around the world (Syvitski et al., 2005; 2022). To understand the relative and combined impacts of these changes, it is crucial to study long-term records of suspended-sediment fluxes (Milliman and Farnsworth, 2013; Walling and Fang, 2003) that account for circa 90% of total sediment loads (Walling and Fang, 2003). Small to meso-scale catchments (up to 1000 km^2) in mountainous and Mediterranean environments yield large amounts of sediment (Milliman and Syvitski, 1992; Vanmaercke et al., 2011) with important contributions from large-magnitude events (e.g., Gonzalez-Hidalgo et al., 2010; Meybeck et al., 2003). Headwater streams in these environments are often well-coupled to hill-slope sediment sources, making them sensitive to landcover changes (e.g., García-Ruiz et al., 2013; Liébault et al., 2005) and highly responsive to ever more frequent high-intensity rainfall episodes (e.g., Nearing et al., 2004; Ombadi et al., 2023). These conditions lead to the occurrence of highly-concentrated sediment transport events with suspended-sediment concentrations (SSCs) of up to tens or hundreds of grams per liter (e.g., Francke et al., 2008; Gentile et al., 2010; Lenzi et al., 2003; Navratil et al., 2012). In order to study the evolution of highly-dynamic river systems and the role of cumulative human impacts, it is therefore crucial to obtain long-term field measurements of suspended-sediment transport that are both temporally resolved and reliable over a wide range of concentrations.

Suspended-sediment transport in rivers is commonly monitored using turbidity sensors that provide an indirect but continuous measure of SSC. These sensors function based on the scattering and absorbance of emitted light by particles that are in suspension (e.g., Gray and Landers, 2014). The angle at which light is detected provides an important constraint on the range of SSCs that can be monitored (e.g., Sadar, 1998) and the sensitivity of measurements to sediment physical properties such as size and colour. Turbidity sensors may be classified based on their scattering angle (Kitchener et al., 2017): forward scatter (FS) is detected at angles of 0°–90°, with direct transmission at 0°; side scatter (SS) is detected at 90° and is also referred to as nephelometry; and backscatter (BS or OBS) is detected at angles of 90°–180°, typically around 135°. The operational ranges of FS and SS sensors are typically smaller than those of BS sensors but allow for higher precision measurements (e.g., Omar and MatJafri, 2009; Sadar, 1998). Turbidity-based scattering measurements are also sensitive to the size distribution of the suspended particles where the scattering intensity is inversely proportional to particle diameter (Conner and De Visser, 1992; Downing, 2006; Gippel, 1995; Thollet et al., 2013). This sensitivity was shown to vary with scattering angle, with preferential scattering of coarse particles in the forward direction (FS; Huber and Frost, 1998; Kleizen et al., 1995) and a minimum variability in scattering observed for BS at angles near 120° (Boss and Pegau, 2001; Oishi, 1990). Furthermore, BS has also been shown to be sensitive to particle colour, which is related to the reflection of near-infrared light (Hatcher et al., 2000; Sutherland et al., 2000), particle shape (Gibbs, 1978) and particulate organic matter (POM) content (Boss et al., 2004).

Although the previously-mentioned experimental studies provide insight into the dependencies of specific sensors on individual properties of well-constrained material, including ground glass, painted sediment or sediment of uniform size or fraction, their combined effects on the monitoring of SSCs of naturally-occurring sediment have rarely been studied (Jastram et al., 2010). For the quantification of sediment fluxes in rivers, uncertainties resulting from a multitude of dependencies on sediment properties are commonly constrained through deriving sensor-specific turbidity vs. SSC rating curves with locally-sampled suspended sediment (e.g., Landers and Sturm, 2013; Navratil et al., 2011). However, rapidly varying or gradually evolving sediment contributions from different sources within

human-impacted catchments may not be adequately detected, hampering the understanding of relevant geomorphological processes and leading to biased sediment loads (e.g., Warrick et al., 2013).

At high SSC, typically above 10 g/L, there are additional challenges for the interpretation of scattering-based turbidity measurements and the quantification of sediment loads. Measurements may no longer show a linear increase with SSC due to a transition from an idealized single-scattering regime to a multiple-scattering regime (i.e., where the emitted light interacts with multiple particles before being detected) with more prominent light absorbance (Sadar, 1998). With further increases in SSC, the scattering intensity saturates at a maximum level and subsequently decays due to the blockage of the light and shielding of particles, which effectively reduces the scattering volume (Kineke and Sternberg, 1992). This inversion leads to a non-unique relationship between measured turbidity and SSC, i.e., a single turbidity value can correspond to two completely different SSCs (e.g., Felix, 2017; Sadar, 1998). Particularly for highly-concentrated flows, it is challenging to constrain uncertainties in SSC and sediment loads as suspended-sediment samples from high-magnitude sediment transport events may be sparse or unavailable. Most often, there is a need to extrapolate turbidity vs. SSC rating curves constructed for lower concentrations, which is inherently uncertain (e.g., Fettweis et al., 2019; Sun et al., 2001) and even more so under a transitioning scattering regime.

Sensors with combined turbidity signals, i.e., where scattered light is detected at multiple angles, may reduce the sensitivity of measurements to varying sediment properties and extend the monitoring range of SSC (Sadar, 1998). However, very little is publicly known about how they function and how well they perform. Review studies on the functioning of turbidity sensors have thus far focused on the use of individual signals in combination with sediment from a limited number of sources. These include: Merten et al. (2014), who tested three SS and FS sensors with clay, silt and sand mixtures; Rymszewicz et al. (2017), who tested ten SS and BS sensors in the laboratory and field with sediment from a river; Davies-Colley et al. (2021) who tested four SS sensors with natural and artificial material; and Felix (2017), who tested five SS and FS sensors with mostly artificial material. Except for the last study, the experimental work was performed for SSCs up to 6 g/L which, indeed, is rarely exceeded in most rivers (e.g., Tramblay et al., 2010). Only a few field studies payed particular attention to the relatively large uncertainties concerning turbidity measurements at higher SSCs (Crosa et al., 2010; Gentile et al., 2010; Navratil et al., 2011), which, despite their infrequent occurrence, may account for the largest part of sediment yields in highly-erodible catchments, particularly in mountainous and Mediterranean environments (e.g., Meybeck et al., 2003; Navratil et al., 2012). The motivation for this study is to assess the sensitivity of individual- and combined-signal sensors turbidity sensors to physical properties of sediment from various sources and how the sensitivity evolves at high SSCs.

We performed a laboratory study to construct turbidity-based SSC rating curves for the combinations of seven types of turbidity sensors and sediment from ten rivers in the suspended-sediment monitoring program of the French network of Critical Zone Observatories (OZCAR; Gaillardet et al., 2018), complemented with industrially-prepared silica. We intercompared the rating curves and used them to evaluate the functioning of the sensors over a wide range of concentrations from 0.05 to 100 g/L. The results are related to sediment particle size, colour and particulate organic matter content, allowing us to explore their relative contributions to scattering intensities. We discuss the implications of our work for the monitoring of evolving sediment sources and fluxes in dynamic, human-impacted small to meso-scale catchments.

2. METHODS

2.1 Investigated sensors

In this study, we tested seven different types of turbidity sensors that function following the European ISO 7027 (2016) standard. The Hach Lange SOLITAX (e.g., Crosa et al., 2010; Gentile et al., 2010; Némery et al., 2013) and WTW ViSolid (e.g., Esteves et al., 2019; Navratil et al., 2011) sensors are well-adapted for the monitoring of rivers with high sediment loads (more than 10 g/L) and are also used in wider river networks (Haddadchi & Hicks, 2020; Lepage et al., 2022; Skarbøvik et al., 2023). The MJK SuSix (Nord et al., 2020), Observator NEP5000 (Snazelle, 2020) and Campbell Scientific OBS501 (Molénat et al., 2018) are wide-range sensors that were installed at OZCAR monitoring sites, but have not been applied in an extensive manner. The Ponsel is commonly used to monitor suspended sediment, e.g., in agricultural catchments (Grangeon et al., 2021; Vongvixay et al., 2018), but its measurement range is limited to 5 g/L. In addition to the abovementioned commercially-available sensors, we also tested the D&M22 open-source sensor that was recently developed by Droujko and Molnar (2022). Although the last two sensors are not well-suited for the monitoring of high sediment loads, they allow for a more comprehensive intercomparison between sensor types at low SSCs. Specifications of the investigated sensors, including their scattering angles, operational range (in the generic units g/L and NTU, Nephelometric Turbidity Unit, following manufacturer guidelines) and preferential installation, are listed in Table 1. The sensors are shown in a photo of the experimental setup in Figure 1a.

Table 1: Sensor specifications

Sensor	Scattering angle	Range[1]	Output	Submergence depth[2]	Bottom clearing[2]	Sidewall clearing[2]
WTW ViSolid 700 IQ	SS (90°) BS (120°)	0.1–300 g/L SiO_2	analog output from DIQ/S 182 transmitter	4.95 cm	10 cm	10 cm
Hach Lange SOLITAX ts-line sc	SS (90°) BS (140°)	0.001–50 g/L	analog output from SC100 transmitter	2.5 cm (calibration)	30 cm (field) 5 cm (calibration)	10–50 cm
MJK SuSix	6 channels (no angle specification)	0.01–400 g/L SiO_2	analog output from transmitter	0.5 cm	3–8 cm	25 cm
Observator NEP5000	SS (90°) BS (180°)	10–30000 NTU	SDI-12	-	5 cm (calibration)	-
Ponsel	SS (90°)	0.001–4.5 g/L 1–4000 NTU	SDI-12	-	-	5 cm
Campbell Scientific OBS501	SS (90°) BS (125–170°)	0.5–1200 NTU 0.5–4000 NTU	SDI-12	-	-	5 cm (SS) 50 cm (BS)
D&M22 open source	BS (135°) FS (45°)	0.1–4000 NTU	stand-alone	3 cm (fixed)[3]	-	3.5 cm (fixed)[3]

[1]the measurement range and provided units are according to manufacturer specifications, based on sensor type and settings that we used; [2]submergence depth and clearing values are minimum values obtained from the sensor manuals (these values are indicative and may depend on the SSC) [3]the D&M22 open source has a partly-enclosed design that allows for a well-constrained scattering volume

The sensors that we used for this study were temporarily removed from field sites or taken from the shelf. They were not specifically calibrated directly prior to our experiments and differ in terms of (1) the material that was used for their calibration, i.e., formazin or pure silica; (2) whether they have a default manufacturer calibration or site-specific calibration (in the case of the MJK SuSix); and (3) the time since calibration. We chose this starting point for our study, as it most often corresponds to the

practice in the field when comparing and/or combining multiple datasets, and we wanted to avoid measurement discontinuities when re-installing the sensors in the field after the experiments. Any potential shifts in measurement values due to differences in calibration will fall well within the wide range of SSCs (3–4 orders of magnitude) that we investigate.

Based on their functioning, we classify the HL SOLITAX, WTW ViSolid, MJK SuSix and NEP5000 as combined-signal sensors and the OBS501, Ponsel and D&M22 as individual-signal sensors. The combined-signal sensors use underlying scattering signals from multiple angles, e.g., SS and BS, to derive turbidity-based measurements (M) for a wide range of SSCs. Proprietary algorithms are used to derive measured values by means of neural logic approaches (MJK SuSix: user manual, Nord et al., 2020), automatic switching between scattering angles (WTW ViSolid: Hung et al., 2014; Papenmeier, 2012), or the use of a turbidity ratio between scattering angles (Hach Lange: $M = T_{SS}/(cT_{BS})$, where T is turbidity, the subscripts denote the scattering angle and c is a calibration coefficient; Sadar, 1998). A lack of understanding of the internal functioning and processing of these sensors makes it challenging to interpret the variability in obtained measurements. The OBS501 and D&M22 are individual-signal sensors where measurements of multiple scattering angles are provided separately and a combined value can be calculated using a weighted ratio (OBS501: $T_{calc} = T_{BS}(T_{SS}/1200) + T_{SS}(1 - T_{SS}/1200)$, operator's manual equation 8–1) and a multiple linear regression function (D&M22: $T_{calc} = c_1 L_{BS} + c_2 L_{FS} + c_3$, Supplementary materials with Droujko and Molnar (2022) equation 5, where L is a raw measure for light intensity in Hz and c_1, c_2 and c_3 are calibration coefficients). For these sensors, we will assess both the individually-measured signals and the calculated turbidity values. Altogether, the individual-signal sensors that we test cover FS, SS and BS, and allow for a more fundamental understanding of the scattering processes and the interpretation of differences among the tested sensors and sediment from different sources.

FIGURE 1 HERE

2.2 Experimental setup and procedure

The experiments were set in a rigid, flat-bottomed container with a diameter of ~40 cm (Figure 1a). The container was filled with 16 L of tap water (determined based on water mass) and left overnight to allow degassing and adjustment to room temperature. The turbidity sensors were placed in a circular configuration, with the sensor optics ~7 cm from the sidewall and other sensors. The sensor optics were installed 10 cm above the bottom of the container and 4 cm below the water surface. The setup (1) is in line with the prescribed submergence and bottom/sidewall clearance (Table 1); (2) is comparable to field installations, where flow depth may be only a few decimeters and flow conditions may require a fixation close to the bank; and (3) allows us to obtain high SSCs with limited amounts of available sediment. A hand-drill-powered paint mixer was installed in the center of the container and was used to ensure water circulation just above the bottom of the container (Figure 1a).

During experiments, dry sediment from a given source was progressively added to the water in the container to obtain SSCs of circa 0.05, 0.1, 0.2, 0.5, 1, 2, 5, 10, 20, 50 and 100 g/L (given sufficient sediment availability per source, see section 2.3). These concentrations were maintained for at least 5 minutes to obtain representative turbidity-based measurements (see for example Figure 1b). Sensor measurements were recorded at 10-second intervals on a Campbell Scientific CR1000 logger. The data was visualized on the fly, using Campbell Scientific RTMC (Real-Time Monitoring and Control Software), and monitored to ensure that stable and plausible data are recorded. This allowed us to identify any issues with sensors due to connectivity problems, fouling, the effect of bubbles from the mixer, etc. Only the D&M22 operated as a stand-alone sensor and the data was downloaded from a

microSD card after the experiment. For SSCs of 5 g/L and higher, additional manual agitation was performed along the sidewall of the container when evidence of sediment deposition was felt. For the sampling of suspended sediment during the experiment, we refer to section 2.4.

2.3 Sediment sources and physical properties

Sediment was collected from river beds or banks at sites of the French network of long-term environmental research observatories (OZCAR, Gaillardet et al., 2018; and RZA, e.g., Thollet et al., 2021). A map with the locations of the ten sites—nine in Metropolitan France and one in the Amazon basin—is provided in Figure 2a. For the Galabre, river bed sediment deposits from two distinct sediment sources were taken, badlands in molasse and black marl formations. The catchments vary in hydro-sedimentary response associated with catchment size, climatic zone, lithology and land cover (Table 2). For the Auradé, Cladugne, Galabre and Roujan rivers in erodible catchments in the south of France, at least half of the cumulative annual loads are transported at SSCs >6 g/L.

All the collected sediment was oven dried (overnight at 35 °C), gently crushed with a mortar and pestle, and sieved to obtain the <63 µm fraction (Figure 2b). This procedure (which is similar to, e.g., Davies-Colley et al., 2021; and Rymszewicz et al., 2017) allows us to exclude sand, which is not or rarely transported in suspension at the considered sites. We assume that all sediment <63 µm is readily transported in suspension. Due to the limited availability of river bed sediment (of which considerable fractions were discarded following sieving), the maximum SSCs that we could obtain per experiment varied with sediment source (for more than half of the sources, we obtained SSC≥20 g/L; Table 2). We also performed an experiment using industrially-prepared silica (99.2 % SiO_2) which is considered as reference material. We did not use formazin due to its unnatural and poorly constrained scattering properties (Kitchener et al., 2017).

FIGURE 2 HERE

Particle-size distributions of sediment were determined per source using a Fritsch Analysette 22 NanoTec laser particle sizer (moderate sonication, Fraunhofer approximation). The size distribution of the sieved sediment is shown per source in Figure 2c. We consider the 10th percentile of the particle size distribution, D_{10}, as a representative measure for particle diameter that exerts an important control on scattering measurements (we confirm this in section 3.3.2) and allows a clear differentiation among the sediment sources. Following Legout et al. (2013), we used a Konica Minolta 2600d spectrophotometer to quantify sediment colour in the CIE 1976 colour space with L^*, a^*, b^* coordinates that provide a measure for lightness, green-red and blue-yellow, respectively (Figure 2d; the sediment in Figure 2b is sorted according to L^*). The lightness L^* is directly comparable to the Munsell value (Kirillova et al., 2015) that was found to affect BS in Sutherland et al. (2000). For our dataset, we found that the yellowness b^* covaries with redness a^* (Spearman's p=0.01) and only show a^* in Figure 2d. Finally, the relative amount of POM in the sediment was estimated using loss on ignition (4 hours at 500 °C) and is also shown in Figure 2d. Sediment from the Strengbach had the highest organic content, composed of relatively coarse organic litter, and was hydrophobic, which made it difficult to bring into suspension.

Table 2: Overview of sites from which sediment was obtained

River, Observatory	Catchment size	Climate	Land cover	Lithology	Suspended-Sediment Concentration (SSC)				Information
					Field[1]			*Experiment*	
					C_{50}	C_{90}	C_{max}		
Galabre, Draix-Bléone	20 km²	mountainous / Mediterranean	forest, grasslands, badlands	marl	13 g/L	110 g/L	361 g/L	0.05–100 g/L	(Legout et al., 2021; Legout et al., 2013; Poulenard et al., 2012)
				molasse				0.05–100 g/L	
Rhône, OSR	20'058 km²	mountainous / temperate	mountains, agriculture	mixed	0.09 g/L	0.53 g/L	0.92 g/L	0.05–100 g/L	(Masson et al., 2018; Poulier et al., 2019)
Isère, Arc-Isère ZABR	5'570 km²	mountainous	mountains, forest, badlands	schist, calcareous rocks, granite, gneiss	1.4 g/L	9.4 g/L	46.9g/L	0.05–50 g/L	(Antoine et al., 2020; Némery et al., 2013; Thollet et al., 2021)
Claduègne, OHMCV	42 km²	Mediterranean	forest, agriculture, badlands	basalt, limestone, marl	5.9 g/L	25 g/L	26.6 g/L	0.05–50 g/L	(Nord et al., 2017; Uber et al., 2019)
Roujan, OMERE	0.9 km²	Mediterranean	agriculture	marl, limestone	-	-	47 g/L	0.05–20 g/L	(Molénat et al., 2018; Raclot et al., 2009)
Auradé, Auradé	3.2 km²	temperate oceanic	agriculture	molasse	27.8 g/L	95.5 g/L	351 g/L	0.05–10 g/L	(Chaumet et al., 2022; Roussiez et al., 2013; Taghavi et al., 2010)
Madre de Dios, HYBAM	118'459 km²	mountainous / humid tropical	forest	-	-	-	-	0.05–10 g/L	(Armijos et al., 2017; Vauchel et al., 2017)
Strengbach, OHGE	0.8 km²	temperate	forest	granite, gneiss	-	-	2.7 g/L	0.05–10 g/L	(Cotel et al., 2020; Pierret et al., 2018; Viville et al., 2012)
Sélune, AgrHys	777 km²	temperate oceanic	agriculture	granite, schist	0.02 g/L	0.07 g/L	2 g/L	0.05–5 g/L	(Fovet et al., 2020; Ndom et al., 2020)
Louroux, ZA Loire	24 km²	temperate oceanic	agriculture	carbonates, detrital and loess deposits	0.09 g/L	0.53 g/L	2.5 g/L	0.05–2 g/L	(Foucher et al., 2015; Grangeon et al., 2017)

[1] *C_{50}, C_{90}: SSC that is exceeded for 50% and 90% of the cumulative load; C_{max}= maximum recorded SSC; these numbers are indicative and not directly intercomparable as they are based on datasets of variable length, time step, etc.*

2.4 Deriving turbidity-based SSC rating curves

Based on visual inspection of the experimental data, we determined representative values for turbidity-based measurements (units depend on sensor output and settings; Figure 1b). Although more subjective than, e.g., averaging over a certain period, this approach allowed us to avoid anomalous values (such as for the WTW ViSolid in Figure 1b) and account for temporally-variable measurements due to local manual agitation, potential flocculation, differences in sensor response time, etc. The sensors generally exhibited a coherent response and constant measurements during the 5-minute periods per imposed SSC. In Appendix A, we discuss the experiments with Cladugègne, Galabre marl and Isère sediment that showed slightly decreasing measurements with time.

To derive actual SSCs during the experiments, we took suspended-sediment samples (30 mL) that we filtered (glass fiber microfilter 0.7 µm), dried (24 hours at 105 °C) and weighed (in grams with 4 decimal precision). The samples were obtained at the height of the sensor optics at three locations in the container for intended SSCs of 5 g/L and higher. In a later stage, additional suspended-sediment samples were taken for intended SSCs of 0.5–10 g/L during repeated experiments with silica, Rhône and Sélune sediment. These additional experiments were performed in order to verify turbidity-based measurements (using abundantly available silica and Rhône sediment, we verified the general reproducibility of the experiments, and for Sélune sediment, we verified the remarkably high turbidity values that we obtained in the original experiment; see results sections 3.1 and 3.2) and to estimate actual SSCs for mixtures with <5 g/L (see Appendix A). The sampling revealed that sediment was uniformly distributed throughout the container, differences were generally less than ±5%, enabling the direct comparison between sensors. The sampled SSCs were 50–100% of the intended value, based on the introduced sediment mass and known water volume, and varied considerably with sediment source, intended SSC and the effect of manual agitation; see Appendix A for details, including sampled particle size. In the results, turbidity-based measurements (in NTU, g/L or Hz) are presented against imposed SSC derived from sampled SSCs.

To analyze the variability of the sensor measurements with sediment from different sources, we fitted power-law, $M = c_1 C^d$, and linear rating curves, $M = kC + c_2$, where M is the turbidity-based measured value, C is the SSC, c_1 and c_2 are fitting constants, d is an exponent close to 1, and k is the specific turbidity (e.g., Bright and Mager, 2020), i.e., the mean increase in M associated with an increase in C of 1 g/L for the fitted range. We account for differences in measured values (e.g., Rymszewicz et al., 2017) and units (g/L and NTU) among the sensors, by using the coefficient of variation (CV; standard deviation divided by mean) to assess sensor variability and by using normalized specific turbidity, k_n (through dividing the fitted k per sediment source by the maximum k found per sensor, similar to e.g., Downing, 2006), for the correlation with natural physical properties of river sediment. To accommodate the relatively small number of sediment sources and the variability in M vs. C relationships among the sensors, we use the nonparametric Spearman's rank correlation to assess the relationships between k_n and D_{10}, L^*, a^*, b^* and POM (i.e., no prior assumption of normally distributed and linearly related data).

3. RESULTS

3.1 Combined-signal turbidity sensors

The Hach Lange SOLITAX turbidity-based SSC measurements show near-linear increases with the imposed SSC (Figure 3a, with $M = C$ indicated for reference). The values for a given SSC may vary with a factor of 5 with sediment source, but this variability is relatively constant across the entire range of considered concentrations. The lowest values were measured for the Isère sediment, which is both relatively coarse and dark coloured (low values for L^* and a^*, Figure 2).

The WTW ViSolid turbidity-based SSC measurements of silica show a continuous power-law trend with an exponent d that is slightly less than 1 (Figure 3b; the exponent corresponds to the slope in the log-log plot). For naturally-occurring river sediment, the increases in measured values with imposed SSC show slightly deviating trends among the investigated sources. For SSCs <0.5 g/L, the trends are systematically steeper than that of silica. No representative value could be established for sediment from several rivers due to highly-fluctuating measurements (see for example Figure 1b). Even though we could establish measured SSC values below 0.1 g/L, this value marks the minimum limit of the prescribed sensor operation range (Table 1). For SSCs >10 g/L, the trends of natural sediment sources diverge and become less steep (this is not the case for silica). The declining trends are most prominent for both relatively coarse and dark-coloured sediment; we will elaborate on this in section 3.3.2. In the case of the Isère and Galabre marl sediment, the measurements flatten off at values of 10–20 g/L.

The MJK SuSix SSC measurements show consistent near-linear increases with imposed SSC, with only a slight discontinuity in the trends at ~5 g/L (Figure 3c). The dispersion among the measured values is within a factor of 5 and slightly smaller than that for the HL SOLITAX (only near the minimum imposed SSC of 0.05 g/L is there an indication for a slightly increased dispersion). At high SSCs of 50–100 g/L, the dispersion among the measurements of different sediment sources is particularly small. Unlike the HL SOLITAX and WTW ViSolid, silica does not lead to the highest SSC measurements with the MJK SuSix as Sélune SSC measurements are noticeably higher.

The Observator NEP5000 shows composite turbidity vs. SSC relationships with two distinct ranges (Figure 3d). First, for measured turbidity values up to 2500 NTU (indicated by the transition line), corresponding to a sampled SSC of 10–20 g/L, the measurements show a log-transformed sinusoidal trend. Similar to the MJK SuSix, Sélune SSC measurements are noticeably higher in this range than sediment from the other sources; we will also observe this for BS measurements in section 3.3. Second, for turbidity measurements higher than 2500 NTU, the trends become steeper again. In this range, the dispersion among the measurements of different sediment sources is very similar to that found for the WTW ViSolid (Figure 3b).

FIGURE 3 HERE

3.2 Individual-signal turbidity sensors

The measurements of the Ponsel SS sensor show consistent near-linear relationships with imposed SSC up to ~5 g/L (Figure 4a, b), which is in line with the operational range provided by the manufacturer (Table 1). The measurements in g/L describe a continuous curve that peaks near a sampled value of 5–10 g/L before decreasing with a further increase in SSC. Despite a manufacturer-prescribed maximum of 4000 NTU (Table 1), the turbidity increases to a value of 7999 NTU which is maintained in the range of 30–50 g/L before decreasing in a similar manner as the g/L measurements. The used NTU cutoff value ensures a near-linear response for sediment from different sources within the sensor's operational range, at the cost of slightly limiting the maximum SSC that can be measured, as shown in g/L measurements for SSC in the range of 1–5 g/L.

The Campbell Scientific OBS501 SS (side scatter) measurements show near-linear turbidity vs. SSC relationships up to 1200 NTU which corresponds to ~2 g/L (Figure 4c). This is the default threshold value where the OBS501 ratio measurement transitions from SS to BS (backscatter) measurements (see section 2.1). The OBS501 BS measurement maintains a near-linear response up to ~5 g/L, with Sélune sediment showing the highest values in this range (this was also observed for the MJK SuSix and NEP5000), and the measurements saturate near 10 g/L. For imposed SSCs >10 g/L, both the SS

and BS show a sharp decrease in NTU values. The BS turbidity measurements show a consistent power-law decay at high SSCs and considerable variability among sediment sources that is larger than that for SS.

The D&M22 open-source sensor FS (forward scatter) light intensity measurements show a power-law relationship with imposed SSC over a very limited range up to 1 g/L (Figure 4e; turbidity values are in Hz which is the unit of the raw output signal of the light detector). The measurement values for silica are considerably higher in this range and subsequently show a power-law decay trend in the range of 0.5–20 g/L, which is not observed for river sediment. The BS sensor shows a response that is very similar to that of the OBS501 with a power-law relationship that flattens off near 5 g/L (Figure 4f).

FIGURE 4 HERE

The variability among measurements for different sediment sources at low SSCs and the maximum extent of the range with near-linear response were very similar for the OBS501 SS and BS measurements. Consequently, combining these measurements using the manufacturer-provided weighted ratio does not lead to a markedly different turbidity vs. SSC relationship (Figure 5a; we limited SS to 1200 NTU to avoid erroneous negative values). Due to the similarity in response, T_{SS}/T_{BS} remains relatively constant, within a factor 0.4–4 (Figure 5c), but may provide an indication for whether measurements are in the rising part of the turbidity vs. SSC rating curve, typically T_{SS}>T_{BS}, or in the falling (inverted) part, typically T_{BS}>T_{SS}. The exact T_{SS}/T_{BS} ratio varies with sediment source, e.g., for the Rhône and Isère where T_{SS}/T_{BS} remains above 1 in both the rising and the falling part of the curve, and determining this transitional value is hampered by maximum turbidity values that are imposed for SS and BS (Figure 4c, d). Once the falling part of the turbidity vs. SSC rating curve is constrained, a decay function can be used to estimate SSC based on BS (or SS) measurements.

The combination of the D&M22 open-source FS and BS signals, following the function provided by the developer, provides a near-linear response in turbidity (Figure 5b). Near 5 g/L, however, the scatter of the calculated turbidity among the sediment sources is likely to be larger than would be the case when only the BS signal was used (Figure 4f). The ratio function T_{FS}/T_{BS} allows the elimination of the saturation and inversion effect that is present in both individually-measured signals. The ratio shows a systematically decreasing trend with imposed SSC that can be described using two power law functions that transition between 1–2 g/L for the investigated river sediment (fitted by eye in Figure 5d). The ratio reveals that FS consistently saturates and decays more rapidly with SSC than BS, which allows the exploitation of the entire response curve for the direct quantification of SSC up to 20 g/L.

FIGURE 5 HERE

3.3 Turbidity-based SSC rating curves

3.3.1 Rating curve variability per sensor

We derived equations of the power-law and linear turbidity-based rating curves per sediment source for the SSC ranges 0.05–1 g/L, for all sensors, and 0.05–100 g/L, for the wide-range combined-signal sensors, and provide these in Appendix B. The obtained rating curves allow the quantification of relative differences among the sediment sources and to make first-order estimates of SSC in the corresponding rivers, although sensor- and site-specific uncertainties are not considered. For the low SSC range, the 1 g/L maximum limit is taken such that we only address the near-linear response

range of the sensors and exclude any saturation and inversion effects at higher SSCs (e.g., Sélune sediment; Figure 4a). The fitting parameters, which are summarized per sensor in Table 3, confirm that the sensors exhibit a near-linear response to SSC as previously seen in Figures 3 and 4. Power-law exponents d (fitted slope in log-log plots) are generally in the range of 0.9–1.1, except for the WTW ViSolid and NEP5000 combined signals at low SSCs and the raw FS and BS signals of the D&M22. With d close to 1, we may consider linear rating curves for further analysis (Table 3). The CV values of the specific turbidity k (fitted M value at C=1 g/L in log-log plots) are comparable between the combined and individual signals at low SSCs. FS performs slightly better than BS for the D&M22 and SS performs slightly better than BS for the OBS501. For the OBS501, the CV of the calculated signal is lower than that of the individual SS and BS signals, indicating their complementarity.

Table 3: Turbidity rating curve fitting parameters per sensor for river sediment (excluding silica)

	Power-law rating curve exponent *d*		**Linear rating curve specific turbidity *k***	
Sensor	*0.05–1 g/L*	*0.05–100 g/L*	*0.05–1 g/L*	*0.05–100 g/L*
HL SOLITAX	1.06±0.08	1.06±0.04	CV=0.53	CV=0.41
WTW ViSolid	1.43±0.28	0.92±0.18	CV=0.49	CV=0.74
MJK SuSix	0.98±0.09	0.97±0.06	CV=0.48	CV=0.44
NEP5000	1.22±0.14	0.90±0.15	CV=0.46	CV=0.64
Ponsel SS NTU	0.94±0.11		CV=0.49	
Ponsel SS g/L	0.93±0.09		CV=0.5	
OBS501 SS	1.03±0.08		CV=0.43	
OBS501 BS	0.92±0.09		CV=0.57	
OBS501 SS, BS	0.97±0.08		CV=0.38	
D&M22 FS	0.56±0.04		CV=0.26	
D&M22 BS	0.69±0.06		CV=0.44	
D&M22 FS, BS	0.87±0.08		CV=0.56	

CV= coefficient of variation

3.3.2 Rating curve dependency on sediment properties

Through normalizing the specific turbidity per sensor, we can explore the scattering sensitivity to sediment physical properties among the sensors and their scattering angles. For low SSCs in the range of 0.05–1 g/L, the normalized specific turbidities, k_n, of all sensors show an inverse relationship with particle size (Figure 6a). The relationship is the strongest and most significant when considering smaller than median (D_{50}) particles, with an optimum near D_{10} (Figure 6b). The SS signals show the highest correlation with particle size ($p<0.01$), followed by BS ($0.01\leq p<0.05$) and FS ($p\geq0.05$). The significance of the relationships of the calculated k_n values with particle size for the OBS501 (SS, BS) and D&M22 (FS, BS) lies between those of the underlying individual signals. The MJK SuSix and NEP5000 combined-signal sensors have p-values similar to those of the SS sensors, while the p-values of WTW ViSolid and HL SOLITAX are similar to those of BS and FS sensors, respectively.

FIGURE 6 HERE

For simplicity, we used a simple linear correlation to relate k_n to D_{10} (Figure 7a). Due to the relatively limited number of considered sediment sources and uncertainties in k_n of the order ±0.1 (associated with sparse sampling at SSCs less than 5 g/L, Appendix C), it is not opportune to derive a more complex function. We do note that the data tentatively suggests a negative power-law relationship with an exponent as small as -1 (Figure 7a; $k_n \propto D_{10}^{-1}$ is added for reference; Downing, 2006), particularly due to the relatively high k_n values for Sélune sediment and silica (although the latter is not included in the statistical analysis due to its artificial nature). The correlations are maintained up to 2 g/L, except for WTW ViSolid and OBS501 (SS, BS) which are no longer significant, and up to 5 g/L

for Ponsel SS NTU and g/L ($p<0.01$) and HL SOLITAX ($p\leq0.05$). In addition to the inverse relation with particle size, a weak positive correlation was found between k_n and the colour parameter b^* in the range of 0.05–1 g/L for BS sensors (Table C1). No significant correlation was found between k_n and a^* (Figure 7b), L^* (not shown) or POM (shown as point size in Figure 7).

FIGURE 7 HERE

When considering the entire investigated SSC range of 0.05–100 g/L, the k_n values of the combined-signal sensors (except for the MJK SuSix) no longer significantly correlate with particle size (Figure 7c). These sensors do show a significant relationship between k_n and a^* (Figure 7d) and, to a lesser extent, between k_n and b^* (Table C1). The value of k_n increases with sediment redness a^*, which is most prominent for WTW ViSolid and NEP5000 combined signals (Figure 7d), and can be directly related to the large spread in turbidity measurements at high SSCs (Figure 3b, d). Note that the k_n for silica does not fit in the trend obtained for the investigated river sediment. No significant relationships were found with L^* or POM.

4. DISCUSSION

4.1 Turbidity sensor calibration and effective operational range

In contrast to earlier review studies (e.g., Davies-Colley et al., 2021; Rymszewicz et al., 2017), we did not calibrate the investigated sensors with formazin directly prior to our experiments. The NTU values that such a calibration would yield are somewhat arbitrary (Davies-Colley et al., 2021; Kitchener et al., 2017) and were found to be manufacturer rather than scattering-mechanism dependent (Rymszewicz et al., 2017). The calibration step, from scattering intensity to NTU, was considered an obsolete and potentially detrimental intermediary step when quantifying site-dependent river SSC from scattering intensity (Downing, 2006; Droujko and Molnar, 2022). To avoid addressing turbidity sensor performance under specific artificial conditions, we considered a wide range of sediment sources and SSCs in our experiments such that we can evaluate sensor response more generally.

When comparing turbidity-based measurements with imposed SSCs of industrially-prepared silica and those of naturally-occurring river sediment, there are considerable differences in the effective SSC range that can be monitored. For instance, the upper SSCs limit of the Ponsel SS NTU individual signal is less than 1 g/L for silica (and is expected to be even lower for the finer formazin) while for natural river sediment, SSCs up to ~5 g/L may be monitored (Figure 4b). The use of silica or formazin as a reference material may give an erroneous nominal sensor operational range that is typically shifted to lower SSCs due to the fine particle size of these materials. Furthermore, sensor calibration with pure silica will not necessarily be suitable when applying it to natural sediment mixtures whose turbidity-based SSC rating curves may be described by a completely different function, e.g., the D&M22 FS signal (Figure 4e) or the WTW ViSolid combined signal (Figure 3b). In the latter case, both high and low SSCs may be underestimated by up to an order of magnitude with respect to the continuous power-law rating curve for silica. Although the WTW ViSolid combined-signal has a theoretical operational range of 0.1–300 g/L (Table 2), in practice, the range varies with sediment source and is rather of the order of 0.5–50 g/L (Figure 3b). Sensor calibration with industrially-prepared material may therefore be misleading in terms of both effective sensor operational range and the form of the rating curve.

The use of combined-signal scattering measurements may enable turbidity measurements for a wide range of SSCs that reach well above 10 g/L. For the sensors that we investigated, this is, however,

only the case for the HL SOLITAX and MJK SuSix combined signals that show rating curves that are consistent among the different sources and over an SSC range of 3–4 orders of magnitude (Figure 3b, c). Although we have little understanding of how the signals are combined internally to derive a turbidity value, it is clear that the effective operational ranges of the underlying signals must be complementary such that a continuous rating curve may be established; in the case of the MJK SuSix, the 6-channel sensor optics is likely to ensure this continuity. In the case of the Observator NEP5000, however, there is insufficient overlap in the range of the underlying SS and BS signal and/or they are combined inadequately. The result is that the sensor shows an intermediate plateau, which, we speculate, is related to the saturation of the SS signal before transitioning to the BS signal with an associated decay function at high SSCs (Figure 3d). This turbidity plateau, which leads to large uncertainties in the quantification of intermediate SSCs (5–20 g/L), is prominent for naturally-occurring river sediment but not visible for fine-grained industrially-prepared material such as pure silica.

When seeking to extend the operational SSC range of turbidity sensors by means of the combination of signals from different scattering angles, there should not be too much overlap between the signals, which is the case for the relatively similar SS and BS signals of the OBS501 (Figure 4c, d). Although their ratio allows the distinction of the rising and falling range of the turbidity-based SSC rating curves, the transition between these ranges is not ambiguous (Figure 5c). The complementary D&M22 FS and BS signals do exhibit systematically different saturation and decay rates, which enabled us to obtain a monotonically decreasing turbidity ratio (where the common saturation and inversion effect of the signals cancel out) that covers the entire turbidity response curve (Figure 5d). Following a turbidity-ratio approach, a wider range of SSCs may be monitored than the rating curve provided by the developers, which was focused on applications that required the precise quantification of low SSCs in NTUs (Droujko and Molnar, 2022). Thus, besides the complementarity of signals, the function that is used to combine these and its intended application range are of the essence when quantifying SSC. These findings emphasize the merit of undisclosed individual scattering signals, that are not truncated at imposed maximum values (such as for the OBS501 SS and BS, and Ponsel SS NTU individual signals); and user-specified computation of turbidity-based values that may be adapted to the sensor response to locally available sediment. We have shown that a simple, low-cost multiple-signal sensor (Droujko and Molnar, 2022) has the potential to quantify a wide range of SSCs using a turbidity-ratio approach with a performance that is similar to or better than some commercial combined-signal sensors.

4.2 Turbidity sensor sensitivity to sediment properties

4.2.1 Scattering sensitivity to particle size for SSCs <5 g/L

We observed turbidity-based measurements per sensor that were within one order-of-magnitude differences among the sediment sources per sensor (Figure 3, 4). These differences are relatively small when considering the multitude of sediment physical properties that may affect scattering intensity. Given the range and variability of the properties that we investigated, order-of-magnitude differences in turbidity may be expected due to particle size (Figure 2c; Downing, 2006) and colour (Figure 2d; Sutherland et al., 2000) alone, while additional effects of particle shape, roughness, refractive index, etc. are also expected to have a significant impact (e.g., Bunt et al., 1999). Through the use of sediment from various rivers rather than synthetically-produced material, we could assess the combined impact of natural sediment properties, but it remains challenging to attribute the individual contributions of individual properties.

The measurements of the individual-signal sensors showed a negative correlation with particle size of river sediment for SSCs up to 1–5 g/L (Figure 6, 7). The most significant correlation of the normalized

specific turbidity, k_n, with particle size, was found for the smallest particle fractions as quantified with D_{10} (Figure 6). The correlation of k_n with D_{10} was the strongest for SS sensors and indicated a negative power-law function with an exponent in the range -1 to 0. The measurement sensitivity to particle size is in line with experiments by Gippel (1995; exponent -0.5) and an inverse relation that is predicted with scattering theory (e.g., Downing, 2006; exponent -1). The correlation of k_n with D_{10} was least significant for D&M22 FS, where the decrease in scattering intensity with increasing particle size is expected to be counteracted by the preferential forward scattering of coarser sediment fractions (e.g., Huber and Frost, 1998). For BS sensors, the correlation of k_n with D_{10} was similar to that of SS but less strong, which may be attributed to an additional dependency on sediment colour as k_n also correlates weakly with b^* (Table C1). For SSCs up to nearly 1 g/L, fine silica suspensions do not yield the highest BS turbidity values (Figure 4d, f) as is the case for the SS sensors (Figure 4a-c). This is remarkable because silica has the smallest particles and highest expected reflectivity of near-infrared light, related to its white colour (Downing, 2006). Based on our data, we can only infer the effect of another particle property, which may covary with b^* and has opposite effects on SS and BS such as particle shape where spherical particles enhance SS while plate-shaped particles enhance BS (Gibbs, 1978). These observations illustrate the difficulty of applying theoretical and laboratory-derived scattering dependencies to the natural properties of river sediment.

The investigated combined-signal sensors show a variability in measurements among sediment sources and a particle-size sensitivity that is similar to those of individual-signal sensors at low SSCs (Table 3 and Figure 6). The disclosed combination of signals results in differences in the particle size dependency per sensor (Figure 6) but does not appear to lead to a reduction in measurement variability or, inadvertently, introduce added uncertainty. Only for the OBS501 we observe a significant reduction in the variability of the measurements associated with the combination of signals (Table 3). Therefore, the use of signals from multiple scattering angles may reduce sensor sensitivity to sediment physical properties, although this is by no means a guarantee (this was also the case for the extension of sensor operational range, see section 4.1).

4.2.2 Scattering sensitivity to sediment colour for SSCs >5 g/L

With increasing SSC in the range of 1–10 g/L, individual FS, SS and BS turbidity measurements saturate and subsequently decrease again (Figure 4) due to a transition in scattering processes, i.e., from single to multiple scattering and increased shielding of grains (Kineke and Sternberg, 1992; Sadar, 1998). In this transition range, we may also expect a change in signal sensitivity to particle size, colour, etc. For the combined-signal sensors, we find that the normalized specific turbidity, k_n, correlates strongly with redness, a^*, when we consider the entire SSC range of 0.05–100 g/L (Figure 7d), which leads to a notable scatter in turbidity measurements from different sources for SSCs >5 g/L (Figure 3b, d). We did not find a correlation between k_n and lightness, L^*, which we might have expected following experiments by Sutherland et al. (2000) and field observations by Voichick and Topping (2014), although they used single-signal sensors based on BS and SS, respectively, and not a combination of signals. The mechanism of near-infrared light reflection that Sutherland et al. (2000) found may also be valid in our case, as both L^* and a^* provide a measure for the reflectance of light at the long-wavelength end of the visible spectrum. At high SSCs, the relative amount of light reflection and absorbance due to particle colour may become increasingly important as light is scattered multiple times before reaching a detector. Although we established that colour parameter a^* may be related to order-of-magnitude variability in different combined-signal turbidity measurements, we cannot exclude the covariance with underlying sediment physical properties such as, e.g., particle shape, roughness or refractive index (Bunt et al., 1999). Further dedicated experiments are needed to clarify the nature and implications of the underlying mechanisms that lead to the observed relations.

4.2.3 Covarying sediment physical parameters

Studies that consider the relative and combined effects of the variability in sediment properties on turbidity-based measurements at a river monitoring station (Jastram et al., 2010) or between different catchments (Lewis et al., 2007) are relatively rare. With river sediment from eleven sources, we provide an experimental basis to explore the variability and sensitivity of sensor measurements beyond the sensor- and site-specific application. Besides relating natural properties of river sediment to (specific) turbidity, it is important to consider the correlations among the properties, such as the positive covariance between a^* and b^* ($p<0.01$) that we found. Similar to turbidity, sediment colour is affected by particle properties and how they affect light reflectance and scatter (e.g., Torrent and Barrón, 1993). L^* has been shown to correlate inversely with particle size for sediment in the Claduègne and Galabre catchments that we considered (Legout et al., 2013; Uber et al., 2019). In the latter catchment, a^* also correlated inversely with particle size. Such a relationship (that we did not find in our dataset; Figure 2d), could yield a strengthened dependency of turbidity on sediment source. I.e., finer and, at the same time, redder particles may lead to enhanced turbidity values. In such a case, the contribution of colour could be mistakenly attributed to particle size or vice-versa. More complex is the case of POM content and particle size, which may exhibit a positive relationship (Jastram et al., 2010) or an inverse relationship (Bright et al., 2020). Note that there is also a potential methodological concern as loss on ignition may not only be due to POM content but also due to residual moisture contained by fine fractions (Grove and Bilotta, 2014). It is therefore difficult to generalize the effect of particle physical properties and their relative contributions to scattering intensity without an integral overview of sediment physical parameters and, ideally, chemical composition (e.g., Horowitz, 2009). This requires the widespread and systematic analysis of suspended-sediment samples, and the instream monitoring of complementary turbidity scattering signals and other techniques such as acoustic backscatter (e.g., Agrawal et al., 2019; Pearson et al., 2021) and spectrometer absorbance (Sehgal et al., 2022), which may be used to quantify particle size or carbon content (major constituent of POM).

4.3 Turbidity sensor application in the field

4.3.1 Monitoring catchment sediment source dynamics

Even when the precise effects of sediment physical properties on turbidity measurements are unknown, different signals or sensors may be used to derive information on sediment provenance (e.g., Landers and Sturm, 2013) in rapidly changing catchments. For example, the MJK SuSix shows relatively little variability in measurements among sediment sources across the entire range of SSCs (Figure 3c), while the Observator NEP5000 shows a marked dependency on colour at high SSCs (Figure 3b, 6b). A ratio between the measurements of these sensors may provide a proxy for temporal changes in the relative contributions of sediment sources in dynamic catchments. This is particularly effective for small catchments with distinctive erodible sediment sources (badlands) and highly-concentrated flows, such as in the considered Galabre (light-coloured molasses and black marl; Figure 2b) and Claduègne rivers (for both rivers, more than 50% of the sediment load is transported at SSCs >5 g/L; Table 2), where sediment source contributions vary strongly on event and intra-event basis (Legout et al., 2013; Uber et al., 2019). In larger meso-scale catchments, SSCs are generally lower and short-term temporal changes in sediment colour are expected to be relatively small due to the contributions of various sediment sources. However, subtle changes in sediment source contributions may go unnoticed, e.g., due to long-term changes in sediment export associated with permafrost degradation (Lafrenière and Lamoureux, 2019) or farmland abandonment (García-Ruiz and Lana-Renault, 2011), or due to basin response in a period following extreme flooding (e.g., Rainato et al., 2021) but also following rapid deforestation for agriculture (Valentin et al., 2008) or wildfires (Gould et al., 2016). For river basin management, it is crucial to know to what extent

changes in turbidity measurements reflect changes in active sediment sources and/or changes in suspended-sediment concentrations. In addition to intermittent sampling, the combined application of complementary turbidity signals or sensors may provide a continuous and highly-resolved means to assess direct and indirect human impacts on sediment export.

4.3.2 Quantifying event-based suspended-sediment loads

The observed operational range, variability with sediment source and sensitivity to sediment physical properties that we investigated may indicate sensor suitability to monitor sediment fluxes for a given catchment with a characteristic hydro-sedimentary response (basin connectivity, distinct sediment sources, etc.). The turbidity-based SSC rating curves that we obtained (Appendix B) may be used to assess the sensitivity and potential uncertainties in SSCs associated with: (1) different types of signals and sensors (Rymszewicz et al., 2017); (2) temporally-varying sediment sources within a catchment (e.g., Landers and Sturm, 2013; Navratil et al., 2012); and (3) the intercomparison between catchments, e.g., for sediment budget calculation (e.g., Guillon et al., 2018; Misset et al., 2019; Orwin and Smart, 2004) or sediment yield purposes (e.g., Haddadchi and Hicks, 2020; Skarbøvik et al., 2023). The absolute values obtained with the rating curves do not provide a measure of sensor performance and cannot be directly used as alternative locally-derived rating curves to quantify SSC in the field. Our results contain uncertainties associated with sediment preparation (obtaining suspended sediment from river bed deposits), sampling (potential loss of sediment during filtering and loss of organic material during drying), particle settling and/or flocculation (Appendix A), experimental boundary conditions (installation constraints, ambient light, water temperature and chemistry) and long-term sensor performance (sensor drift, fouling, etc.). These uncertainties are however subordinate to the differences that we found among the sensors and the range of SSC that is monitored.

To illustrate the potential implications of the observed differences among the sensors for field applications, we perform a thought experiment using two fictive SSC histories (sediment graphs) with Rhône sediment covering the ranges of 0.05–5 g/L and 0.5–50 g/L. Figure 8 (a, c) illustrates the variability in measurements among the sensors that register in g/L with respect to the imposed SSC in the considered ranges. Such variability can be largely reduced using rating curves with locally-derived sediment, which is particularly important for the highest SSCs. Notably, for the WTW ViSolid, SSCs below 10 g/L are overestimated while SSCs above 10 g/L are underestimated (Figure 8a, c) due to a colour-related saturation effect (section 4.2.2). The Ponsel SS, which is not suited to monitor high SSCs, shows a completely different sediment graph with an inverse peak near the maximum imposed SSC and two small peaks near 5 g/L (Figure 8c). Saturation plateaus (e.g., Rasmussen et al., 2009) or inverse peaks may be recognized and assessed using complementary measurements in field applications (e.g., Voichick et al., 2018), including multiple individual scattering signals (e.g., OBS501 and D&M22) or flow stage. This will, however, not always be the case in situations where sediment transport dynamics are complex, making the quantification of sediment loads at and beyond the saturation plateau inherently uncertain.

In our thought experiment, we subsequently consider a hydrograph with the same form as the sediment graph, i.e., the sediment graph is a direct (i.e., no time-delay), linear transformation of the hydrograph (e.g., Asselman, 1999; Syvitski et al., 2000; Walling, 1977). This allows us to assess the effect of applying rating curves with locally-derived sediment on cumulative transported loads (Figure 8b, d). Because high SSCs coincide with high discharges, any error in the estimated SSC (with respect to the imposed amount) will have a disproportionally strong impact on total sediment loads, e.g., the time-averaged error of the MJK SuSix is +29%, while the error in the peak and cumulative loads are respectively +47.5% and +46.7% (Figure 8c, d). Accurate quantification of highly-

concentrated flows is therefore crucial to monitor sediment fluxes in dynamic river systems. This applies to the role of high-magnitude events associated with climatic extremes, particularly in mountainous and Mediterranean catchments (e.g., Francke et al., 2008; García-Ruiz et al., 2013; Lenzi et al., 2003; López-Tarazón et al., 2009; Navratil et al., 2012; Poulenard et al., 2012), but also to (ephemeral) streams in semi-arid to arid catchments (e.g., Alexandrov et al., 2009; Benkhaled et al., 2014). In addition, the monitoring of highly-concentrated flows is essential to evaluate the downstream impacts of controlled sediment release flows from hydropower installations (e.g., Antoine et al., 2020; Crosa et al., 2010).

FIGURE 8 HERE

In our laboratory experiments and fictive sediment transport histories, we do not account for changes in particle size distribution with SSC (Appendix A) or discharge. In a river setting, local shear stresses will affect the settling (e.g., Ferguson & Church, 2004) and (re-)suspension of particles (e.g., Haddad et al., 2022), and the extent to which flocculation processes may occur (e.g., Maltauro et al., 2023). Under transport-limited conditions in rivers, particle size distributions typically coarsen with increasing flow competence, leading to further underestimation of sediment loads in large-magnitude flow events (e.g., Grangeon et al., 2012; Lenzi and Marchi, 2000; Wass and Leeks, 1999). Conversely, supply-limited conditions in rivers can lead to inverse relationships between particle size and discharge where fine suspended sediment is eroded from river banks or hill slopes (Landers and Sturm, 2013; Pfannkuche and Schmidt, 2003; Slattery and Burt, 1997). In this case, an underestimation in SSC may be (partly) compensated by particle size dynamics during flow events. Although POM content may be associated with flocculation (Droppo and Ongley, 1994) and lead to reduced turbidity values (Bright and Mager, 2016; Slaets et al., 2014), its effect is minimal during high discharges (e.g., Lee et al., 2019) and high SSCs (Madej, 2015; Masson et al., 2018; Némery et al., 2013) in dynamic river systems. In general, besides the physically-interrelated sediment properties of particle size, colour, etc. (section 4.2.3), we also need to consider hydro-geomorphological relations among sediment availability, discharge, particle size, etc., during sediment transport events (e.g., Lepesqueur et al., 2019). This calls for a comprehensive understanding of the dynamics and evolution of sediment sources and transport conditions to quantify the impacts of human-induced changes in the landscape and climate on sediment yield from erodible small to meso-scale catchments.

5. CONCLUSIONS

We experimentally investigated turbidity sensors with varying scattering angles and with combined signals with sediment from various rivers. Sensors with multiple signals may allow the accurate quantification of SSC for the entire investigated range of 0.05–100 g/L, although the effective range was found to depend on both the sensor and the sediment source. The operational ranges of individual signals, most often SS and BS, can be similar to such an extent that when they are combined, the effective monitoring range is not enhanced but the sensitivity to (temporally varying) sediment physical properties may be slightly reduced. On the other hand, the overlap between the signals and/or the functions that are used to combine the signals may be inadequate, resulting in a non-continuous turbidity-based SSC rating curve with enhanced uncertainty near the transition between the signals, typically in the range of 1–10 g/L. This exemplifies the need for multiple, individually-accessible scattering signals and user-specified turbidity calculation (rather than disclosed, automatically processed measurements), which may allow low-cost sensors to perform as well as or better than commercial combined-signal sensors.

At low SSCs, below 1–5 g/L, the specific turbidities of SS and BS measurements were sensitive to the smallest particle fractions (D_{10}), which is in line with previous studies (e.g., Downing, 2006). At higher SSCs, above 5–10 g/L, measurements from BS and combined-signal sensors become increasingly dependent on particle colour, as quantified as CIE a^* and, to a lesser extent, b^*, but not to L^* that is comparable to the Munsell value (Sutherland, et al., 2000). We associate this with a transition from idealized single scattering to multiple scattering with enhanced light absorption, which leads to an observed shift in the sensitivity of turbidity-based measurements with SSC from particle size to particle colour. However, the relative impacts of sediment physical parameters, including particle size, colour, shape, etc., are difficult to assess and generalize due to covariance among these parameters in naturally-occurring river sediment. Their combined effects lead to a variability in turbidity-based measurements with sediment sources that is generally within one order of magnitude in the effective operational range of the investigated sensors.

Our results emphasize the need to assess turbidity sensor performance with locally-obtained river sediment rather than industrially-prepared materials such as pure silica or formazin. Complementary scattering measurements may be used to constrain sediment source dynamics and/or highly fluctuating SSCs in erodible small to meso-scale catchments. Our work illustrates typical uncertainties and potential errors that need to be considered when monitoring sediment transfer and assessing the relative and combined effects of human-induced changes in the landscape and climate.

ACKNOWLEDGMENTS

This project was funded by the French network of Critical Zone Observatories OZCAR, contract n°EB2021-2103449904. Additional support was provided by the French National Research Agency (ANR) grant ANR-18-CE01-0019-01 (DEAR project). The Institute of Environmental Geosciences (IGE) in Grenoble hosted MB for this study and provided the necessary laboratory facilities and equipment. We acknowledge Olivier Alemany, Sophie Darfeuil, and Laurent Oxarango for their assistance with laboratory equipment and Celine Duwig for the logistics and transport of sediment. We thank two anonymous reviewers for their detailed and constructive comments, which led to the improvement of this manuscript.

APPENDIX A: SAMPLED SSC AND PARTICLE SIZE

More than 100 suspended-sediment samples were taken during the course of the experiments to verify concentrations and ensure sensor intercomparability. Sampling started ~1 minute after adding the sediment to the water for (intended) SSCs of 5 g/L and higher (for Louroux only at the maximum obtained SSC of 2 g/L, Table 2). The time between consecutive samples for a given SSC was ~30 seconds. Samples were taken at the height of the optics directly beside the HL SOLITAX, WTW ViSolid and OBS501 sensors. For three repeated experiments, with silica, Rhône and Sélune sediment, larger samples were taken to ensure sufficient sediment at lower SSCs: 90 mL at 2 g/L, 135 mL at 1 g/L and 180 mL at 0.5 g/L. During these experiments, we verified that the measured data corresponded to that of the original experiments.

Differences in sampled SSC between the three locations in the container were generally within ±5% (more than 90% of the samples) and only samples for Isère sediment for intended SSCs of 5 g/L were ±10–15%. Part of the observed variability can be attributed to a minor but systematic decrease in SSC of approximately 2% per minute between the samples taken at the three locations (i.e., SSCs from samples that were consistently taken first, besides the HL SOLITAX, were 2% lower than those taken last, besides the OBS501). Given the small variability in sampled SSC at the three locations, we consider the sediment to be uniformly distributed throughout the container.

SSCs from the three sampling locations are averaged and shown as a percentage of the intended SSC per experiment in Figure A1. The experimental setup and procedure allowed for the suspension of 50–100% of the inserted sediment, which varied considerably between experiments with sediment from different sources and during the course of each experiment. When solely relying on the paint mixer for SSCs up to 5 g/L, a modest decrease in sampled SSC is observed during the experiments with silica, Sélune and Rhône sediment. For an intended SSC of 5 g/L, the sampled SSCs appear to be inversely related to particle size, where coarser sediment fractions have higher settling velocities (e.g., Ferguson & Church, 2004) and are most likely to deposit. With the onset of (additional) manual agitation, performed to re-suspend the deposited sediment that was felt along the edge of the container for SSCs equal to or greater than 5 g/L, we found a general increase in the sampled SSC. For intended SSCs of 20–100 g/L, we found 80–100% of the sediment in suspension. Galabre marl sediment formed an exception with merely ~60% of the inserted sediment that was sampled, which we attribute to flocculation (we explain this at the end of this Appendix).

FIGURE A1 HERE

For sediment from sources for which no sampling was performed at SSCs <5 g/L, we estimated the sampled SSC with the average percentage for the range of 5–20 g/L (Figure A1). The resulting uncertainty in imposed SSC may be conservatively estimated to be ±10%, based on the error for

763 silica, Sélune and Rhône for SSC of 0.5, 1 and 2 g/L. The impact of this uncertainty on observed
764 statistical relations between k_n and sediment physical properties is discussed in Appendix C. The
765 uncertainty in imposed SSCs does not affect the intercomparison among the investigated sensors, as
766 any bias is the same for all sensors.

767 For each experiment, we determined the particle size distribution of suspended-sediment samples
768 obtained at the maximum SSC to explore the role of size-selective deposition processes. The
769 differences between the imposed (sieved) and sampled particle size distributions are generally
770 limited (Table A1). For six of the twelve experiments, the difference was within 10% for D_{10}. In two
771 experiments, with Cladugne and Isère sediment, the difference in particle size was of the order of
772 100%. In these cases, the sampled sediment was considerably finer than the original sediment that
773 was introduced into the container, indicating the settling out of the coarsest fraction and, hence, the
774 fining of the sampled sediment. Note that the amounts of deposition were not excessive in both
775 cases, ~90% for an intended SSC of 50 g/L (Figure A1).

776 *Table A1: Imposed (sieved) and sampled particle size D_{10} and D_{50}*

Sediment	Imposed		Sampled		Difference	
	D_{10} [µm]	D_{50} [µm]	D_{10} [µm]	D_{50} [µm]	D_{10} [%]	D_{50} [%]
Silica	0.73	2.09	0.74	2.26	-1%	-8%
Gal. Mol.	1.37	10.60	1.37	9.85	0%	8%
Roujan	1.60	12.03	2.38	14.88	-33%	-19%
Gal. Marl	1.60	16.56	1.44	13.83	11%	20%
Sélune	1.69	15.84	1.80	14.61	-6%	8%
Madre Dios	2.10	15.15	2.00	13.37	5%	13%
Auradé	2.18	16.65	1.55	11.19	41%	49%
Cladugne	2.76	21.53	1.09	8.13	**153%**	**165%**
Rhône	3.60	21.07	3.51	19.83	2%	6%
Strengbach	4.53	26.95	4.27	25.29	6%	7%
Louroux	4.94	31.68				
Isère	7.31	31.79	3.68	25.19	**98%**	26%

777 *[1]sampled amounts of Louroux suspended sediment were insufficient to obtain a (reliable) particle size*
778 *distribution*

779 For Galabre marl, Cladugne and (particularly) Isère sediment, we observed slightly decreasing trends
780 in turbidity-based measurements and sampled SSCs during the 5-minute periods. Based on the
781 particle size distributions of the sampled Cladugne and Isère sediment, we can attribute this
782 observation to the preferential deposition of the coarsest fractions (even though the sensor is less
783 sensitive to these fractions). For Galabre marl sediment, we observe only a relatively modest
784 difference in particle size between sieved and sampled sediment, but this does exclude the
785 occurrence of flocculation (e.g., Gibbs and Wolanski, 1992) during the experiments as flocs are not
786 maintained after filtering, drying and sonication. We attribute the proposed flocculation to the high
787 clay mineral content in the marl. When determining representative turbidity values per experiment
788 and imposed SSC, we sought to minimize the effects of settling particles and flocculation, i.e., values
789 near the beginning of the 5-minute periods.

APPENDIX B: TURBIDITY-BASED SSC RATING CURVES

Table B1: linear rating curves (Spearman's p<0.05) and the number of data points used (n in brackets) in the range of 0.05–1 g/L for the combined-signal sensors

Sediment	HL SOLITAX	WTW ViSolid	MJK SuSix	NEP5000
Silica	-	M=3.61C+0.128 (n=5)	M=2.22C+0.023 (n=5)	M=1111C+14 (n=5)
Gal. Mol.	M=0.56C+0.016 (n=5)	-	M=2.03C+0.014 (n=5)	M=894C+6 (n=5)
Roujan	M=0.42C+0.032 (n=5)	-	M=1.52C+0.069 (n=5)	M=700C+14 (n=5)
Gal. Marl	M=0.61C-0.004 (n=5)	-	M=2.01C+0.008 (n=5)	M=930C-14 (n=5)
Sélune	M=1.29C-0.031 (n=5)	-	M=3.94C-0.021 (n=5)	M=1731C-7 (n=5)
Madre Dios	M=0.42C+0.002 (n=5)	-	M=1.44C+0.013 (n=5)	M=622C+9 (n=5)
Auradé	M=0.57C+0.015 (n=5)	-	M=1.95C+0.06 (n=5)	M=843C+20 (n=5)
Claduègne	M=0.46C-0.005 (n=5)	M=1.98C-0.053 (n=5)	M=1.47C-0.01 (n=5)	M=647C-22 (n=5)
Rhône	M=0.32C-0.004 (n=5)	-	M=1.1C+0.008 (n=5)	M=584C-12 (n=5)
Strengbach	M=0.47C-0.003 (n=5)	-	M=1.27C+0.011 (n=5)	-
Louroux	-	M=1.25C-0.044 (n=5)	M=1.13C+0.01 (n=5)	-
Isère	-	-	M=0.98C+0.012 (n=5)	-

Table B2: power-law rating curves (Spearman's p<0.05) and the number of data points used (n in brackets) in the range of 0.05–1 g/L for the combined-signal sensors

Sediment	HL SOLITAX	WTW ViSolid	MJK SuSix	NEP5000
Silica	-	M=0.55C^0.85 (n=5)	M=0.34C^0.94 (n=5)	M=3.07C^1 (n=5)
Gal. Mol.	M=-0.16C^1.11 (n=5)	-	M=0.34C^1.06 (n=5)	M=3.04C^1.21 (n=5)
Roujan	M=-0.31C^0.9 (n=5)	-	M=0.2C^0.88 (n=5)	M=2.93C^1.14 (n=5)
Gal. Marl	M=-0.18C^1.08 (n=5)	-	M=0.27C^0.93 (n=5)	M=3.08C^1.25 (n=5)
Sélune	M=0.1C^1.1 (n=5)	-	M=0.57C^0.99 (n=5)	M=3.28C^1.1 (n=5)
Madre Dios	M=-0.34C^1.07 (n=5)	-	M=0.15C^0.95 (n=5)	M=2.85C^1.07 (n=5)
Auradé	M=-0.21C^0.97 (n=5)	-	M=0.31C^0.94 (n=5)	M=2.96C^0.99 (n=5)
Claduègne	M=-0.29C^1.16 (n=5)	M=0.28C^1.11 (n=5)	M=0.17C^1.03 (n=5)	M=2.87C^1.34 (n=5)
Rhône	M=-0.53C^0.97 (n=5)	-	M=0.05C^0.99 (n=5)	M=2.84C^1.27 (n=5)
Strengbach	M=-0.31C^1.07 (n=5)	-	M=0.22C^1.19 (n=5)	-
Louroux	-	M=0.17C^1.32 (n=5)	M=0.02C^0.91 (n=5)	-
Isère	-	-	M=-0.03C^0.91 (n=5)	-

Table B3: linear rating curves (Spearman's p<0.05) and the number of data points used (n in brackets) in the range of 0.05–1 g/L for the individual-signal sensors

Sediment	Ponsel SS NTU	Ponsel SS g/L	OBS501 SS	OBS501 BS	D&M22 FS	D&M22 BS
Silica	M=8230C-34 (n=5)	M=2.37C-0.02 (n=5)	M=1539C-48 (n=5)	M=551C-11 (n=5)	-	M=21109C+524 (n=5)
Gal. Mol.	M=3165C+49 (n=5)	M=0.92C (n=5)	M=647C-3 (n=5)	M=320C+4 (n=5)	M=95522C+25575 (n=5)	M=12100C+1194 (n=5)
Roujan	M=2921C+118 (n=5)	M=0.81C+0.02 (n=5)	M=503C+13 (n=5)	M=242C+11 (n=5)	M=96916C+29764 (n=5)	M=9291C+1340 (n=5)
Gal. Marl	M=3737C+51 (n=5)	M=1.03C+0.01 (n=5)	M=575C+1 (n=5)	M=230C+6 (n=5)	M=125806C+20377 (n=5)	M=10210C+967 (n=5)
Sélune	-	M=1.79C-0.03 (n=5)	M=1118C-21 (n=5)	M=642C-1 (n=5)	M=139400C+24176 (n=5)	M=21737C+1419 (n=5)
Madre Dios	M=2265C+67 (n=5)	M=0.61C+0.02 (n=5)	M=416C+4 (n=5)	M=158C+11 (n=5)	M=77840C+22941 (n=5)	M=6996C+1265 (n=5)
Auradé	M=3076C+58 (n=5)	M=0.85C+0.01 (n=5)	M=624C+1 (n=5)	M=293C+9 (n=5)	M=89947C+26639 (n=5)	M=11393C+1378 (n=5)
Claduègne	M=2215C+2 (n=5)	M=0.6C (n=5)	M=460C-8 (n=5)	M=225C (n=5)	M=85215C+16700 (n=5)	M=8467C+710 (n=5)
Rhône	M=1736C+118 (n=5)	M=0.47C+0.03 (n=5)	M=389C+1 (n=5)	M=176C+5 (n=5)	M=77284C+13920 (n=5)	M=7442C+784 (n=5)
Strengbach	M=1896C+80 (n=5)	M=0.55C+0.01 (n=5)	M=414C-2 (n=5)	M=187C+3 (n=5)	M=67261C+17550 (n=5)	M=6951C+853 (n=5)
Louroux	-	M=0.53C (n=5)	M=365C (n=5)	M=168C+3 (n=5)	M=98628C+10715 (n=5)	M=8148C+534 (n=5)
Isère	M=1584C+14 (n=5)	M=0.39C+0.01 (n=5)	M=262C+1 (n=5)	M=117C+4 (n=5)	M=55314C+10692 (n=5)	M=5860C+606 (n=5)

Table B4: power-law rating curves (Spearman's p<0.05) and the number of data points used (n in brackets) in the range of 0.05–1 g/L for the individual-signal sensors

Sediment	Ponsel SS NTU	Ponsel SS g/L	OBS501 SS	OBS501 BS	D&M22 FS	D&M22 BS
Silica	M=3.91C^1 (n=5)	M=0.37C^1.03 (n=5)	M=3.18C^1.13 (n=5)	M=2.71C^1.02 (n=5)	-	M=4.27C^0.81 (n=5)
Gal. Mol.	M=3.54C^1.04 (n=5)	M=-0.03C^1.02 (n=5)	M=2.83C^1.08 (n=5)	M=2.53C^1.01 (n=5)	M=5.1C^0.61 (n=5)	M=4.13C^0.79 (n=5)
Roujan	M=3.48C^0.89 (n=5)	M=-0.09C^0.91 (n=5)	M=2.72C^0.95 (n=5)	M=2.41C^0.88 (n=5)	M=5.12C^0.57 (n=5)	M=4.02C^0.69 (n=5)
Gal. Marl	M=3.53C^0.88 (n=5)	M=-0.03C^0.9 (n=5)	M=2.76C^0.98 (n=5)	M=2.34C^0.86 (n=5)	M=5.1C^0.56 (n=5)	M=3.97C^0.64 (n=5)
Sélune	-	-	M=3.03C^1.05 (n=5)	M=2.78C^0.95 (n=5)	M=5.17C^0.59 (n=5)	M=4.32C^0.75 (n=5)
Madre Dios	M=3.38C^0.95 (n=5)	M=-0.22C^0.89 (n=5)	M=2.61C^0.95 (n=5)	M=2.22C^0.8 (n=5)	M=5C^0.53 (n=5)	M=3.9C^0.62 (n=5)
Auradé	M=3.5C^0.96 (n=5)	M=-0.08C^0.93 (n=5)	M=2.79C^0.98 (n=5)	M=2.48C^0.91 (n=5)	M=5.07C^0.56 (n=5)	M=4.1C^0.72 (n=5)
Claduègne	M=3.35C^1.02 (n=5)	M=-0.25C^0.96 (n=5)	M=2.66C^1.07 (n=5)	M=2.34C^0.97 (n=5)	M=4.99C^0.6 (n=5)	M=3.94C^0.74 (n=5)
Rhône	M=3.26C^0.8 (n=5)	M=-0.35C^0.75 (n=5)	M=2.6C^1 (n=5)	M=2.26C^0.91 (n=5)	M=4.92C^0.58 (n=5)	M=3.88C^0.68 (n=5)
Strengbach	M=3.4C^1.08 (n=5)	M=-0.17C^1.07 (n=5)	M=2.72C^1.22 (n=5)	M=2.36C^1.11 (n=5)	M=4.9C^0.52 (n=5)	M=3.87C^0.68 (n=5)
Louroux	-	-	M=2.58C^1.02 (n=5)	M=2.21C^0.91 (n=5)	M=4.93C^0.57 (n=5)	M=3.84C^0.67 (n=5)
Isère	M=3.21C^0.98 (n=5)	M=-0.45C^0.83 (n=5)	M=2.41C^0.97 (n=5)	M=2.05C^0.84 (n=5)	M=4.73C^0.48 (n=5)	M=3.73C^0.62 (n=5)

Table B5: linear and power-law rating curves (Spearman's p<0.05) and the number of data points used (n in brackets) in the range of 0.05–100 g/L

Sediment	OBS501 SS, BS	D&M22 FS, BS	OBS501 SS, BS	D&M22 FS, BS
Silica	M=512C-15 (n=5)	M=653C+43 (n=5)	M=2.63C^1 (n=5)	M=2.87C^0.88 (n=5)
Gal. Mol.	M=242C+9 (n=5)	M=477C+17 (n=5)	M=2.43C^0.96 (n=5)	M=2.73C^0.99 (n=5)
Roujan	M=170C+16 (n=5)	M=389C+25 (n=5)	M=2.28C^0.81 (n=5)	M=2.64C^0.88 (n=5)
Gal. Marl	M=224C+27 (n=5)	M=479C+8 (n=5)	M=2.39C^0.7 (n=5)	M=2.68C^0.93 (n=5)
Sélune	M=497C+6 (n=5)	M=841C+5 (n=5)	M=2.67C^0.91 (n=5)	M=2.92C^0.97 (n=5)
Madre Dios	M=121C+15 (n=5)	M=332C+14 (n=5)	M=2.14C^0.75 (n=5)	M=2.54C^0.88 (n=5)
Auradé	M=224C+13 (n=5)	M=454C+22 (n=5)	M=2.38C^0.85 (n=5)	M=2.69C^0.89 (n=5)
Cladugne	M=149C+6 (n=5)	M=379C+2 (n=5)	M=2.2C^0.92 (n=5)	M=2.59C^1.01 (n=5)
Rhône	M=134C+6 (n=5)	M=331C+7 (n=5)	M=2.15C^0.88 (n=5)	M=2.54C^0.96 (n=5)
Strengbach	M=130C+7 (n=5)	M=358C+3 (n=5)	M=2.18C^0.93 (n=5)	M=2.66C^1.18 (n=5)
Louroux	M=142C+2 (n=5)	M=330C+2 (n=5)	M=2.14C^0.93 (n=5)	M=2.53C^0.99 (n=5)
Isère	M=112C+2 (n=5)	M=241C+3 (n=5)	M=2.04C^0.91 (n=5)	M=2.38C^0.95 (n=5)

Table B6: linear rating curves (Spearman's p<0.05) and the number of data points used (n in brackets) in the range of 0.05–100 g/L for the combined-signal sensors

Sediment	HL SOLITAX	WTW ViSolid	MJK SuSix	NEP5000
Silica	M=0.93C+1.76 (n=9)	M=1.8C+1.33 (n=10)	M=1.01C+5.09 (n=11)	M=1113C-537 (n=9)
Gal. Mol.	M=0.5C+1.46 (n=11)	M=0.52C+5.27 (n=9)	M=1.31C+2.35 (n=11)	M=323C+719 (n=11)
Roujan	M=0.63C-0.02 (n=9)	M=0.92C+1.3 (n=8)	M=1.45C+0.15 (n=9)	M=286C+278 (n=9)
Gal. Marl	M=0.6C+0.47 (n=11)	M=0.26C+3.24 (n=10)	M=3.33C-2.65 (n=10)	M=85C+705 (n=11)
Sélune	M=1.17C+0.04 (n=7)	M=2.53C+0.94 (n=5)	M=2.66C+0.42 (n=7)	M=615C+342 (n=7)
Madre Dios	M=0.65C-0.08 (n=8)	M=1.25C+0.91 (n=5)	M=1.41C+0.12 (n=8)	M=252C+234 (n=8)
Auradé	M=0.64C-0.01 (n=8)	M=1.28C+1.07 (n=6)	M=1.3C+0.41 (n=8)	M=251C+354 (n=8)
Cladugne	M=0.51C+0.16 (n=10)	M=0.55C+2.02 (n=10)	M=1.52C-0.72 (n=10)	M=233C+253 (n=10)
Rhône	M=0.37C+0.32 (n=11)	M=0.26C+3.14 (n=10)	M=1.16C+0.95 (n=11)	M=91C+590 (n=11)
Strengbach	M=0.7C-0.05 (n=8)	-	M=1.33C+0.04 (n=8)	M=306C+173 (n=5)
Louroux	M=0.36C+0 (n=5)	M=1.28C-0.05 (n=6)	M=1.1C+0.02 (n=6)	M=510C-10 (n=5)
Isère	M=0.27C+0.05 (n=9)	M=0.19C+2.77 (n=5)	M=1.15C-0.84 (n=10)	M=41C+478 (n=9)

802 *Table B7: power-law rating curves (Spearman's p<0.05) and the number of data points used (n in brackets) in the range of 0.05–100 g/L for the combined-signal sensors*

Sediment	HL SOLITAX	WTW ViSolid	MJK SuSix	NEP5000
Silica	M=0.06C^1.03 (n=9)	M=0.52C^0.82 (n=10)	M=0.33C^0.91 (n=11)	M=2.99C^0.92 (n=9)
Gal. Mol.	M=-0.21C^1.03 (n=11)	M=0.39C^0.72 (n=9)	M=0.25C^0.95 (n=11)	M=2.79C^0.88 (n=11)
Roujan	M=-0.23C^1.01 (n=9)	M=0.11C^1.06 (n=8)	M=0.24C^0.92 (n=9)	M=2.73C^0.87 (n=9)
Gal. Marl	M=-0.21C^1.04 (n=11)	M=0.05C^0.9 (n=10)	M=0.34C^1.02 (n=10)	M=2.65C^0.76 (n=11)
Sélune	M=0.08C^1.08 (n=7)	M=0.54C^1.16 (n=5)	M=0.53C^0.94 (n=7)	M=3.08C^0.89 (n=7)
Madre Dios	M=-0.29C^1.11 (n=8)	M=0.29C^0.85 (n=5)	M=0.18C^0.98 (n=8)	M=2.69C^0.87 (n=8)
Auradé	M=-0.2C^0.99 (n=8)	M=0.3C^0.92 (n=6)	M=0.27C^0.88 (n=8)	M=2.8C^0.78 (n=8)
Claduègne	M=-0.36C^1.08 (n=10)	M=0.14C^0.89 (n=10)	M=0.15C^1 (n=10)	M=2.58C^0.94 (n=10)
Rhône	M=-0.43C^1.04 (n=11)	M=0.01C^0.86 (n=10)	M=0.07C^1.01 (n=11)	M=2.52C^0.82 (n=11)
Strengbach	M=-0.26C^1.13 (n=8)	-	M=0.11C^1.08 (n=8)	M=2.64C^0.95 (n=5)
Louroux	M=-0.4C^1.1 (n=5)	M=0.13C^1.28 (n=6)	M=0.03C^0.92 (n=6)	M=2.77C^1.31 (n=5)
Isère	M=-0.6C^1.05 (n=9)	M=0.003C^0.7 (n=5)	M=0.01C^0.96 (n=10)	M=2.37C^0.81 (n=9)

803

APPENDIX C: RATING CURVE DEPENDENCY ON PARTICLE PROPERTIES: STATISTICS AND UNCERTAINTY

In Table C1 we provide the Spearman's r- and p-values associated with the statistical relations between k_n and sediment physical properties D_{10}, a^*, and b^*. For L^* and POM we found no statistically significant relations (p>0.05).

Table C1: Spearman's r- and p-values

	k_n* vs. *D_{10}		***k_n* vs. *a^****		***k_n* vs. *b^****	
Sensor	*0.05–1 g/L*	*0.05–100 g/L*	*0.05–1 g/L*	*0.05–100 g/L*	*0.05–1 g/L*	*0.05–100 g/L*
HL SOLITAX	r=-0.64, p<0.05	-	-	r=0.70, p<0.05	-	
WTW ViSolid	r=-0.79, p<0.05	-	-	**r=0.85, p<0.01**	-	r=0.67, p<0.05
MJK SuSix	**r=-0.86, p<0.01**	r=-0.65, p<0.05	-	-	-	
NEP5000	**r=-0.87, p<0.01**	-	-	**r=0.79, p<0.01**	-	r=0.65, p<0.05
Ponsel SS NTU	**r=-0.85, p<0.01**		-		-	
Ponsel SS g/L	**r=-0.86, p<0.01**		-		-	
OBS501 SS	**r=-0.84, p<0.01**		-		-	
OBS501 BS	r=-0.73, p<0.05		-		r=0.66, p<0.05	
OBS501 SS, BS	r=-0.82, p<0.01*		-		-	
D&M22 FS	-*		-		-	
D&M22 BS	r=-0.75, p<0.01*		-		r=0.65, p<0.05**	
D&M22 FS, BS	r=-0.72, p<0.05		-		r=0.66, p<0.05**	

*k_n: normalized specific turbidity; D_{10} particle diameter; a^*, b^*: CIE colour parameters; highly-significant relations are indicated in bold; *p<0.05 and **p>0.05 based on the uncertainty analysis*

Uncertainties of ±10% in the imposed SSCs <5 g/L propagate linearly into k_n uncertainties of ±0.1 for the range of 0.05–1 g/L and may therefore affect the statistical relations in Figures 6 and 7 (a, b), and Table C1 (uncertainties in k_n values for the entire SSC range of 0.05–100 g/L are negligible). We performed a Monte-Carlo-based uncertainty analysis through perturbing k_n values with a random factor drawn from a normal distribution with a mean of 1 and a standard deviation of 0.1. The resulting median r- and p-values were subsequently determined for more than 100 simulations. The previously established relations between k_n vs. D_{10} (Figures 6 and 7a) are maintained, although the uncertainty propagation yielded a marginal increase in p-values (in the case of calculated OBS501 SS, BS and the D&M22 BS measurements, this led to a significance of p<0.05 rather than p<0.01; Table C1). Only for D&M22 FS there was a decrease in p-value, resulting in a significant k_n vs. D_{10} relation of r=-0.62, p<0.05. For the D&M22 BS and calculated D&M22 FS, BS measurements, the relation of k_n vs. b^* was no longer significant (p>0.05) when accounting for uncertainties (Table C1).

REFERENCES

Agrawal, Y. C., Portsmith, H., Dana, D., & Mikkelsen, O. (2019). *Super-Turbidity Meter: LISST-AOBS Combines Optical Turbidity with Acoustics.* Paper presented at the Proceedings of the 38th IAHR World Congress, Panama City, Panama.

Alexandrov, Y., Cohen, H., Laronne, J. B., & Reid, I. (2009). Suspended sediment load, bed load, and dissolved load yields from a semiarid drainage basin: A 15-year study. *Water Resources Research, 45*(8). doi: 10.1029/2008WR007314

Antoine, G., Camenen, B., Jodeau, M., Némery, J., & Esteves, M. (2020). Downstream erosion and deposition dynamics of fine suspended sediments due to dam flushing. *Journal of Hydrology, 585*, 124763. doi: 10.1016/j.jhydrol.2020.124763

Armijos, E., Crave, A., Espinoza, R., Fraizy, P., Santos, A. L. M. R. D., Sampaio, F., . . . Filizola, N. (2017). Measuring and modeling vertical gradients in suspended sediments in the Solimões/Amazon River. *Hydrological Processes, 31*(3), 654-667. doi: 10.1002/hyp.11059

Asselman, N. E. M. (1999). Suspended sediment dynamics in a large drainage basin: the River Rhine. *Hydrological Processes, 13*(10), 1437-1450. doi: 10.1002/(SICI)1099-1085(199907)13:10<1437::AID-HYP821>3.0.CO;2-J

Benkhaled, A., Higgins, H., Chebana, F., & Necir, A. (2014). Frequency analysis of annual maximum suspended sediment concentrations in Abiod wadi, Biskra (Algeria). *Hydrological Processes, 28*(12), 3841-3854. doi: 10.1002/hyp.9880

Boss, E., & Pegau, W. S. (2001). Relationship of light scattering at an angle in the backward direction to the backscattering coefficient. *Applied Optics, 40*(30), 5503-5507. doi: 10.1364/AO.40.005503

Boss, E., Pegau, W. S., Lee, M., Twardowski, M., Shybanov, E., Korotaev, G., & Baratange, F. (2004). Particulate backscattering ratio at LEO 15 and its use to study particle composition and distribution. *Journal of Geophysical Research: Oceans, 109*(C1). doi: 10.1029/2002JC001514

Bright, C., Mager, S., & Horton, S. (2020). Response of nephelometric turbidity to hydrodynamic particle size of fine suspended sediment. *International Journal of Sediment Research, 35*(5), 444-454. doi: 10.1016/j.ijsrc.2020.03.006

Bright, C. E., & Mager, S. M. (2016). Contribution of particulate organic matter to riverine suspended material in the Glendhu Experimental Catchments, Otago, New Zealand. *Journal of Hydrology (New Zealand), 55*(2), 89-106.

Bright, C. E., & Mager, S. M. (2020). A national-scale study of spatial variability in the relationship between turbidity and suspended sediment concentration and sediment properties. *River Research and Applications, 36*(8), 1449-1459. doi: 10.1002/rra.3679

Bunt, J. A. C., Larcombe, P., & Jago, C. F. (1999). Quantifying the response of optical backscatter devices and transmissometers to variations in suspended particulate matter. *Continental Shelf Research, 19*(9), 1199-1220. doi: 10.1016/S0278-4343(99)00018-7

Chaumet, B., Probst, J.-L., Payré-Suc, V., Granouillac, F., Riboul, D., & Probst, A. (2022). Pond mitigation in dissolved and particulate pesticide transfers: Influence of storm events and seasonality (Auradé agricultural catchment, SW-France). *J Environ Manage, 320*, 115911. doi: 10.1016/j.jenvman.2022.115911

Conner, C. S., & De Visser, A. M. (1992). A laboratory investigation of particle size effects on an optical backscatterance sensor. *Marine Geology, 108*(2), 151-159. doi: 10.1016/0025-3227(92)90169-I

Cotel, S., Viville, D., Benarioumlil, S., Ackerer, P., & Pierret, M. C. (2020). Impact of the hydrological regime and forestry operations on the fluxes of suspended sediment and bedload of a small middle-mountain catchment. *Science of The Total Environment, 743*, 140228. doi: 10.1016/j.scitotenv.2020.140228

Crosa, G., Castelli, E., Gentili, G., & Espa, P. (2010). Effects of suspended sediments from reservoir flushing on fish and macroinvertebrates in an alpine stream. *Aquatic Sciences, 72*(1), 85-95. doi: 10.1007/s00027-009-0117-z

875 Davies-Colley, R., Hughes, A. O., Vincent, A. G., & Heubeck, S. (2021). Weak numerical comparability
876 of ISO-7027-compliant nephelometers. Ramifications for turbidity measurement applications.
877 *Hydrological Processes, 35*(12), e14399. doi: 10.1002/hyp.14399
878 Downing, J. (2006). Twenty-five years with OBS sensors: The good, the bad, and the ugly. *Continental*
879 *Shelf Research, 26*(17), 2299-2318. doi: 10.1016/j.csr.2006.07.018
880 Droppo, I. G., & Ongley, E. D. (1994). Flocculation of suspended sediment in rivers of southeastern
881 Canada. *Water Research, 28*(8), 1799-1809. doi: 10.1016/0043-1354(94)90253-4
882 Droujko, J., & Molnar, P. (2022). Open-source, low-cost, in-situ turbidity sensor for river network
883 monitoring. *Scientific Reports, 12*(1), 10341. doi: 10.1038/s41598-022-14228-4
884 Esteves, M., Legout, C., Navratil, O., & Evrard, O. (2019). Medium term high frequency observation of
885 discharges and suspended sediment in a Mediterranean mountainous catchment. *Journal of*
886 *Hydrology, 568*, 562-574. doi: 10.1016/j.jhydrol.2018.10.066
887 Felix, D. (2017). Experimental investigation on suspended sediment, hydro-abrasive erosion and
888 efficiency reductions of coated Pelton turbines. *VAW-Mitteilungen, 238*.
889 Fettweis, M., Riethmüller, R., Verney, R., Becker, M., Backers, J., Baeye, M., . . . Vereecken, H. (2019).
890 Uncertainties associated with in situ high-frequency long-term observations of suspended
891 particulate matter concentration using optical and acoustic sensors. *Progress in Oceanography,*
892 *178*, 102162. doi: 10.1016/j.pocean.2019.102162
893 Foucher, A., Laceby, P. J., Salvador-Blanes, S., Evrard, O., Le Gall, M., Lefèvre, I., . . . Desmet, M.
894 (2015). Quantifying the dominant sources of sediment in a drained lowland agricultural
895 catchment: The application of a thorium-based particle size correction in sediment fingerprinting.
896 *Geomorphology, 250*, 271-281. doi: 10.1016/j.geomorph.2015.09.007
897 Fovet, O., Ndom, M., Crave, A., & Pannard, A. (2020). Influence of dams on river water-quality
898 signatures at event and seasonal scales: The Sélune River (France) case study. *River Research and*
899 *Applications, 36*(7), 1267-1278. doi: 10.1002/rra.3618
900 Francke, T., López-Tarazón, J. A., Vericat, D., Bronstert, A., & Batalla, R. J. (2008). Flood-based analysis
901 of high-magnitude sediment transport using a non-parametric method. *Earth Surface Processes*
902 *and Landforms, 33*(13), 2064-2077. doi: 10.1002/esp.1654
903 Gaillardet, J., Braud, I., Hankard, F., Anquetin, S., Bour, O., Dorfliger, N., . . . Zitouna, R. (2018).
904 OZCAR: The French Network of Critical Zone Observatories. *Vadose Zone Journal, 17*(1), 180067.
905 doi: 10.2136/vzj2018.04.0067
906 García-Ruiz, J. M., & Lana-Renault, N. (2011). Hydrological and erosive consequences of farmland
907 abandonment in Europe, with special reference to the Mediterranean region – A review.
908 Agriculture, Ecosystems & Environment, 140(3), 317-338. doi: 10.1016/j.agee.2011.01.003
909 García-Ruiz, J. M., Nadal-Romero, E., Lana-Renault, N., & Beguería, S. (2013). Erosion in
910 Mediterranean landscapes: Changes and future challenges. *Geomorphology, 198*, 20-36. doi:
911 10.1016/j.geomorph.2013.05.023
912 Gentile, F., Bisantino, T., Corbino, R., Milillo, F., Romano, G., & Liuzzi, G. T. (2010). Monitoring and
913 analysis of suspended sediment transport dynamics in the Carapelle torrent (Southern Italy).
914 *CATENA, 80*(1), 1-8. doi: 10.1016/j.catena.2009.08.004
915 Gibbs, R. J. (1978). Light scattering from particles of different shapes. *Journal of Geophysical*
916 *Research: Oceans, 83*(C1), 501-502. doi: 10.1029/JC083iC01p00501
917 Gibbs, R. J., & Wolanski, E. (1992). The effect of flocs on optical backscattering measurements of
918 suspended material concentration. *Marine Geology, 107*(4), 289-291. doi: 10.1016/0025-
919 3227(92)90078-V
920 Gippel, C. J. (1995). Potential of turbidity monitoring for measuring the transport of suspended solids
921 in streams. *Hydrological Processes, 9*(1), 83-97. doi: 10.1002/hyp.3360090108
922 Gonzalez-Hidalgo, J. C., Batalla, R. J., Cerdà, A., & de Luis, M. (2010). Contribution of the largest
923 events to suspended sediment transport across the USA. *Land Degradation & Development, 21*(2),
924 83-91. doi: 10.1002/ldr.897

Gould, G. K., Liu, M., Barber, M. E., Cherkauer, K. A., Robichaud, P. R., & Adam, J. C. (2016). The effects of climate change and extreme wildfire events on runoff erosion over a mountain watershed. *Journal of Hydrology, 536*, 74-91. doi: 10.1016/j.jhydrol.2016.02.025

Grangeon, T., Ceriani, V., Evrard, O., Grison, A., Vandromme, R., Gaillot, A., . . . Salvador-Blanes, S. (2021). Quantifying hydro-sedimentary transfers in a lowland tile-drained agricultural catchment. *CATENA, 198*, 105033. doi: 10.1016/j.catena.2020.105033

Grangeon, T., Legout, C., Esteves, M., Gratiot, N., & Navratil, O. (2012). Variability of the particle size of suspended sediment during highly concentrated flood events in a small mountainous catchment. *Journal of Soils and Sediments, 12*(10), 1549-1558. doi: 10.1007/s11368-012-0562-5

Grangeon, T., Manière, L., Foucher, A., Vandromme, R., Cerdan, O., Evrard, O., . . . Salvador-Blanes, S. (2017). Hydro-sedimentary Dynamics of a Drained Agricultural Headwater Catchment: A Nested Monitoring Approach. *Vadose Zone Journal, 16*(12), vzj2017.2005.0113. doi: 10.2136/vzj2017.05.0113

Gray, J. R., & Landers, M. N. (2014). 1.10 - Measuring Suspended Sediment. In S. Ahuja (Ed.), *Comprehensive Water Quality and Purification* (pp. 157-204). Waltham: Elsevier.

Grove, M. K., & Bilotta, G. S. (2014). On the use of loss-on-ignition techniques to quantify fluvial particulate organic carbon. *Earth Surface Processes and Landforms, 39*(9), 1146-1152. doi: 10.1002/esp.3509

Guillon, H., Mugnier, J.-L., & Buoncristiani, J.-F. (2018). Proglacial sediment dynamics from daily to seasonal scales in a glaciated Alpine catchment (Bossons glacier, Mont Blanc massif, France). *Earth Surface Processes and Landforms, 43*(7), 1478-1495. doi: 10.1002/esp.4333

Haddad, H., Jodeau, M., Legout, C., Antoine, G., & Droppo, I. G. (2022). Spatial variability of the erodibility of fine sediments deposited in two alpine gravel-bed rivers: The Isère and Galabre. *CATENA, 212*, 106084. doi: 10.1016/j.catena.2022.106084

Haddadchi, A., & Hicks, M. (2020). Understanding the effect of catchment characteristics on suspended sediment dynamics during flood events. *Hydrological Processes, 34*(7), 1558-1574. doi: 10.1002/hyp.13682

Hatcher, A., Hill, P., Grant, J., & Macpherson, P. (2000). Spectral optical backscatter of sand in suspension: effects of particle size, composition and colour. *Marine Geology, 168*(1), 115-128. doi: 10.1016/S0025-3227(00)00042-6

Huber, E., & Frost, M. (1998). Light scattering by small particles. *Journal of Water Supply: Research and Technology-Aqua, 47*(2), 87-94. doi: 10.2166/aqua.1998.14

Hung, N. N., Delgado, J. M., Güntner, A., Merz, B., Bárdossy, A., & Apel, H. (2014). Sedimentation in the floodplains of the Mekong Delta, Vietnam. Part I: suspended sediment dynamics. *Hydrological Processes, 28*(7), 3132-3144. doi: 10.1002/hyp.9856

ISO 7027 (2016): Water Quality. Determination of Turbidity, Part 1: Quantitative Methods: International Organisation for Standardization Geneva, Switzerland.

Jastram, J. D., Zipper, C. E., Zelazny, L. W., & Hyer, K. E. (2010). Increasing Precision of Turbidity-Based Suspended Sediment Concentration and Load Estimates. *J Environ Qual, 39*(4), 1306-1316. doi: 10.2134/jeq2009.0280

Kineke, G. C., & Sternberg, R. W. (1992). Measurements of high concentration suspended sediments using the optical backscatterance sensor. *Marine Geology, 108*(3), 253-258. doi: 10.1016/0025-3227(92)90199-R

Kirillova, N. P., Vodyanitskii, Y. N., & Sileva, T. M. (2015). Conversion of soil color parameters from the Munsell system to the CIE-L*a*b* system. *Eurasian Soil Science, 48*(5), 468-475. doi: 10.1134/S1064229315050026

Kitchener, B. G. B., Wainwright, J., & Parsons, A. J. (2017). A review of the principles of turbidity measurement. *Progress in Physical Geography: Earth and Environment, 41*(5), 620-642. doi: 10.1177/0309133317726540

Kleizen, H. H., de Putter, A. B., van der Beek, M., & Huynink, S. J. (1995). Particle concentration, size and turbidity. *Filtration & Separation, 32*(9), 897-901. doi: 10.1016/S0015-1882(97)84175-4

Lafrenière, M. J., & Lamoureux, S. F. (2019). Effects of changing permafrost conditions on hydrological processes and fluvial fluxes. *Earth-Science Reviews, 191*, 212-223. doi: 10.1016/j.earscirev.2019.02.018

Landers, M. N., & Sturm, T. W. (2013). Hysteresis in suspended sediment to turbidity relations due to changing particle size distributions. *Water Resources Research, 49*(9), 5487-5500. doi: 10.1002/wrcr.20394

Lee, B. J., Kim, J., Hur, J., Choi, I. H., Toorman, E. A., Fettweis, M., & Choi, J. W. (2019). Seasonal Dynamics of Organic Matter Composition and Its Effects on Suspended Sediment Flocculation in River Water. *Water Resources Research, 55*(8), 6968-6985. Doi: 10.1029/2018WR024486

Legout, C., Freche, G., Biron, R., Esteves, M., Navratil, O., Nord, G., . . . Spadini, L. (2021). A critical zone observatory dedicated to suspended sediment transport: The meso-scale Galabre catchment (southern French Alps). *Hydrological Processes, 35*(3), e14084. doi: 10.1002/hyp.14084

Legout, C., Poulenard, J., Nemery, J., Navratil, O., Grangeon, T., Evrard, O., & Esteves, M. (2013). Quantifying suspended sediment sources during runoff events in headwater catchments using spectrocolorimetry. *Journal of Soils and Sediments, 13*(8), 1478-1492. doi: 10.1007/s11368-013-0728-9

Lenzi, M. A., Mao, L., & Comiti, F. (2003). Interannual variation of suspended sediment load and sediment yield in an alpine catchment. *Hydrological Sciences Journal, 48*(6), 899-915. doi: 10.1623/hysj.48.6.899.51425

Lenzi, M. A., & Marchi, L. (2000). Suspended sediment load during floods in a small stream of the Dolomites (northeastern Italy). *CATENA, 39*(4), 267-282. doi: 10.1016/S0341-8162(00)00079-5

Lepage, H., Gruat, A., Thollet, F., Le Coz, J., Coquery, M., Masson, M., . . . Raimbault, P. (2022). Concentrations and fluxes of suspended particulate matter and associated contaminants in the Rhône River from Lake Geneva to the Mediterranean Sea. *Earth Syst. Sci. Data, 14*(5), 2369-2384. doi: 10.5194/essd-14-2369-2022

Lepesqueur, J., Hostache, R., Martínez-Carreras, N., Montargès-Pelletier, E., & Hissler, C. (2019). Sediment transport modelling in riverine environments: on the importance of grain-size distribution, sediment density, and suspended sediment concentrations at the upstream boundary. *Hydrol. Earth Syst. Sci., 23*(9), 3901-3915. doi: 10.5194/hess-23-3901-2019

Lewis, J., Eads, R., & Klein, R. (2007). *Comparisons of Turbidity Data Collected with Different Instruments*. Retrieved from http://water.usgs.gov/fisp/docs/Tprobe_final_report.pdf

Liébault, F., Gomez, B., Page, M., Marden, M., Peacock, D., Richard, D., & Trotter, C. M. (2005). Land-use change, sediment production and channel response in upland regions. *River Research and Applications, 21*(7), 739-756. doi: 10.1002/rra.880

López-Tarazón, J. A., Batalla, R. J., Vericat, D., & Francke, T. (2009). Suspended sediment transport in a highly erodible catchment: The River Isábena (Southern Pyrenees). *Geomorphology, 109*(3), 210-221. doi: 10.1016/j.geomorph.2009.03.003

Madej, M. A. (2015). Export of fine particulate organic carbon from redwood-dominated catchments. *Earth Surface Processes and Landforms, 40*(11), 1533-1541. doi: 10.1002/esp.3752

Maltauro, R., Stone, M., Collins, A. L., Krishnappan, B. G., & Silins, U. (2023). The effect of shear-dependent flocculation on the multimodality of effective particle size distributions in a gravel-bed river during high flows. *Journal of Soils and Sediments*. doi: 10.1007/s11368-023-03455-5

Masson, M., Angot, H., Le Bescond, C., Launay, M., Dabrin, A., Miège, C., . . . Coquery, M. (2018). Sampling of suspended particulate matter using particle traps in the Rhône River: Relevance and representativeness for the monitoring of contaminants. *Science of The Total Environment, 637-638*, 538-549. doi: 10.1016/j.scitotenv.2018.04.343

Merten, G. H., Capel, P. D., & Minella, J. P. G. (2014). Effects of suspended sediment concentration and grain size on three optical turbidity sensors. *Journal of Soils and Sediments, 14*(7), 1235-1241. doi: 10.1007/s11368-013-0813-0

Meybeck, M., Laroche, L., Dürr, H. H., & Syvitski, J. P. M. (2003). Global variability of daily total suspended solids and their fluxes in rivers. *Global and Planetary Change, 39*(1), 65-93. doi: 10.1016/S0921-8181(03)00018-3

Milliman, J. D., & Farnsworth, K. L. (2013). *River discharge to the coastal ocean: a global synthesis*: Cambridge University Press.
Milliman, J. D., & Syvitski, J. P. M. (1992). Geomorphic/Tectonic Control of Sediment Discharge to the Ocean: The Importance of Small Mountainous Rivers. *The Journal of Geology, 100*(5), 525-544. doi: 10.1086/629606
Misset, C., Recking, A., Legout, C., Valsangkar, N., Bodereau, N., Zanker, S., . . . Borgniet, L. (2019). The Dynamics of Suspended Sediment in a Typical Alpine Alluvial River Reach: Insight From a Seasonal Survey. *Water Resources Research, 55*(12), 10918-10934. doi: 10.1029/2019WR025222
Molénat, J., Raclot, D., Zitouna, R., Andrieux, P., Coulouma, G., Feurer, D., . . . Voltz, M. (2018). OMERE: A Long-Term Observatory of Soil and Water Resources, in Interaction with Agricultural and Land Management in Mediterranean Hilly Catchments. *Vadose Zone Journal, 17*(1), 180086. doi: 10.2136/vzj2018.04.0086
Navratil, O., Esteves, M., Legout, C., Gratiot, N., Nemery, J., Willmore, S., & Grangeon, T. (2011). Global uncertainty analysis of suspended sediment monitoring using turbidimeter in a small mountainous river catchment. *Journal of Hydrology, 398*(3), 246-259. doi: 10.1016/j.jhydrol.2010.12.025
Navratil, O., Evrard, O., Esteves, M., Legout, C., Ayrault, S., Némery, J., . . . Bonté, P. (2012). Temporal variability of suspended sediment sources in an alpine catchment combining river/rainfall monitoring and sediment fingerprinting. *Earth Surface Processes and Landforms, 37*(8), 828-846. doi: 10.1002/esp.3201
Ndom, M., Fovet, O., Crave, A., & Gilliet, N. (2020). *Dynamique fluviale (Volet 1): Flux hydriques, sédimentaires et chimiques [Programme Sélune-Phase pré-arasement. Rapport bilan 2018-2019].* Agence de l'Eau Seine-Normandie.
Nearing, M., Pruski, F. F., & O'Neal, M. R. (2004). Expected climate change impacts on soil erosion rates: A review. *Journal of soil and water conservation, 59*(1), 43-50.
Némery, J., Mano, V., Coynel, A., Etcheber, H., Moatar, F., Meybeck, M., . . . Poirel, A. (2013). Carbon and suspended sediment transport in an impounded alpine river (Isère, France). *Hydrological Processes, 27*(17), 2498-2508. doi: 10.1002/hyp.9387
Nord, G., Boudevillain, B., Berne, A., Branger, F., Braud, I., Dramais, G., . . . Wijbrans, A. (2017). A high space–time resolution dataset linking meteorological forcing and hydro-sedimentary response in a mesoscale Mediterranean catchment (Auzon) of the Ardèche region, France. *Earth Syst. Sci. Data, 9*(1), 221-249. doi: 10.5194/essd-9-221-2017
Nord, G., Michielin, Y., Biron, R., Esteves, M., Freche, G., Geay, T., . . . Mercier, B. (2020). An autonomous low-power instrument platform for monitoring water and solid discharges in mesoscale rivers. *Geosci. Instrum. Method. Data Syst., 9*(1), 41-67. doi: 10.5194/gi-9-41-2020
Oishi, T. (1990). Significant relationship between the backward scattering coefficient of sea water and the scatterance at 120°. *Applied Optics, 29*(31), 4658-4665. doi: 10.1364/AO.29.004658
Omar, A. F. B., & MatJafri, M. Z. B. (2009). Turbidimeter design and analysis: a review on optical fiber sensors for the measurement of water turbidity. *Sensors, 9*(10), 8311-8335.
Ombadi, M., Risser, M. D., Rhoades, A. M., & Varadharajan, C. (2023). A warming-induced reduction in snow fraction amplifies rainfall extremes. *Nature.* doi: 10.1038/s41586-023-06092-7
Orwin, J. F., & Smart, C. C. (2004). Short-term spatial and temporal patterns of suspended sediment transfer in proglacial channels, small River Glacier, Canada. *Hydrological Processes, 18*(9), 1521-1542. doi: 10.1002/hyp.1402
Papenmeier, S. (2012). *Properties and dynamics of suspended load and near-bed fine cohesive sediments in highly impacted estuaries. Case studies from the Weser, Ems and Elbe estuaries (Germany).* Univierstiy of Kiel.
Pearson, S. G., Verney, R., van Prooijen, B. C., Tran, D., Hendriks, E. C. M., Jacquet, M., & Wang, Z. B. (2021). Characterizing the Composition of Sand and Mud Suspensions in Coastal and Estuarine Environments Using Combined Optical and Acoustic Measurements. *Journal of Geophysical Research: Oceans, 126*(7), e2021JC017354. doi: 10.1029/2021JC017354

Pfannkuche, J., & Schmidt, A. (2003). Determination of suspended particulate matter concentration from turbidity measurements: particle size effects and calibration procedures. *Hydrological Processes, 17*(10), 1951-1963. doi: 10.1002/hyp.1220

Pierret, M.-C., Cotel, S., Ackerer, P., Beaulieu, E., Benarioumlil, S., Boucher, M., . . . Probst, A. (2018). The Strengbach Catchment: A Multidisciplinary Environmental Sentry for 30 Years. *Vadose Zone Journal, 17*(1), 180090. doi: 10.2136/vzj2018.04.0090

Poulenard, J., Legout, C., Némery, J., Bramorski, J., Navratil, O., Douchin, A., . . . Esteves, M. (2012). Tracing sediment sources during floods using Diffuse Reflectance Infrared Fourier Transform Spectrometry (DRIFTS): A case study in a highly erosive mountainous catchment (Southern French Alps). *Journal of Hydrology, 414-415*, 452-462. doi: 10.1016/j.jhydrol.2011.11.022

Poulier, G., Launay, M., Le Bescond, C., Thollet, F., Coquery, M., & Le Coz, J. (2019). Combining flux monitoring and data reconstruction to establish annual budgets of suspended particulate matter, mercury and PCB in the Rhône River from Lake Geneva to the Mediterranean Sea. *Science of The Total Environment, 658*, 457-473. doi: 10.1016/j.scitotenv.2018.12.075

Raclot, D., Le Bissonnais, Y., Louchart, X., Andrieux, P., Moussa, R., & Voltz, M. (2009). Soil tillage and scale effects on erosion from fields to catchment in a Mediterranean vineyard area. *Agriculture, Ecosystems & Environment, 134*(3), 201-210. doi: 10.1016/j.agee.2009.06.019

Rainato, R., Martini, L., Pellegrini, G., & Picco, L. (2021). Hydrological, geomorphic and sedimentological responses of an alpine basin to a severe weather event (Vaia storm). *CATENA, 207*, 105600. doi: 10.1016/j.catena.2021.105600

Rasmussen, P. P., Gray, J. R., Glysson, G. D., & Ziegler, A. C. (2009). Guidelines and procedures for computing time-series suspended-sediment concentrations and loads from in-stream turbidity-sensor and streamflow data. *US geological survey techniques and methods, book, 3*, 52.

Roussiez, V., Probst, A., & Probst, J.-L. (2013). Significance of floods in metal dynamics and export in a small agricultural catchment. *Journal of Hydrology, 499*, 71-81. doi: 10.1016/j.jhydrol.2013.06.013

Rymszewicz, A., O'Sullivan, J. J., Bruen, M., Turner, J. N., Lawler, D. M., Conroy, E., & Kelly-Quinn, M. (2017). Measurement differences between turbidity instruments, and their implications for suspended sediment concentration and load calculations: A sensor inter-comparison study. *J Environ Manage, 199*, 99-108. doi: 10.1016/j.jenvman.2017.05.017

Sadar, M. J. (1998). Turbidity science. Technical Information Series—Booklet no. 11. *Hach Co. Loveland CO, 7*(8).

Sehgal, D., Martínez-Carreras, N., Hissler, C., Bense, V. F., & Hoitink, A. J. F. (2022). Inferring Suspended Sediment Carbon Content and Particle Size at High Frequency From the Optical Response of a Submerged Spectrometer. *Water Resources Research, 58*(5), e2021WR030624. doi: 10.1029/2021WR030624

Skarbøvik, E., Gyritia Madsen van't Veen, S., Lannergård, E. E., Wenng, H., Stutter, M., Bieroza, M., . . . Kämäri, M. (2023). Comparing in situ turbidity sensor measurements as a proxy for suspended sediments in North-Western European streams. *CATENA, 225*, 107006. doi: 10.1016/j.catena.2023.107006

Slaets, J. I. F., Schmitter, P., Hilger, T., Lamers, M., Piepho, H.-P., Vien, T. D., & Cadisch, G. (2014). A turbidity-based method to continuously monitor sediment, carbon and nitrogen flows in mountainous watersheds. *Journal of Hydrology, 513*, 45-57. doi: 10.1016/j.jhydrol.2014.03.034

Slattery, M. C., & Burt, T. P. (1997). Particle size characteristics of suspended sediment in hillslope runoff and stream flow. *Earth Surface Processes and Landforms, 22*(8), 705-719. doi: 10.1002/(SICI)1096-9837(199708)22:8<705::AID-ESP739>3.0.CO;2-6

Snazelle, T. T. (2020). Field comparison of five in situ turbidity sensors. No. 2020-1123. US Geological Survey.

Sun, H., Cornish, P. S., & Daniell, T. M. (2001). Turbidity-based erosion estimation in a catchment in South Australia. *Journal of Hydrology, 253*(1), 227-238. doi: 10.1016/S0022-1694(01)00475-9

Sutherland, T. F., Lane, P. M., Amos, C. L., & Downing, J. (2000). The calibration of optical backscatter sensors for suspended sediment of varying darkness levels. *Marine Geology, 162*(2), 587-597. doi: 10.1016/S0025-3227(99)00080-8

Syvitski, J., Ángel, J. R., Saito, Y., Overeem, I., Vörösmarty, C. J., Wang, H., & Olago, D. (2022). Earth's sediment cycle during the Anthropocene. *Nature Reviews Earth & Environment, 3*(3), 179-196. doi: 10.1038/s43017-021-00253-w

Syvitski, J. P., & Kettner, A. (2011). Sediment flux and the Anthropocene. *Philosophical Transactions of the Royal Society A: Mathematical, Physical and Engineering Sciences, 369*(1938), 957-975.

Syvitski, J. P., Morehead, M. D., Bahr, D. B., & Mulder, T. (2000). Estimating fluvial sediment transport: The rating parameters. *Water Resources Research, 36*(9), 2747-2760. doi: 10.1029/2000WR900133

Syvitski, J. P., Vörösmarty, C. J., Kettner, A. J., & Green, P. (2005). Impact of humans on the flux of terrestrial sediment to the global coastal ocean. *science, 308*(5720), 376-380.

Taghavi, L., Probst, J.-L., Merlina, G., Marchand, A.-L., Durbe, G., & Probst, A. (2010). Flood event impact on pesticide transfer in a small agricultural catchment (Montoussé at Auradé, south west France). *International Journal of Environmental Analytical Chemistry, 90*(3-6), 390-405. doi: 10.1080/03067310903195045

Thollet, F., Le Coz, J., Antoine, G., François, P., Saguintaah, L., Launay, M., & Camenen, B. (2013). Influence de la granulométrie des particules sur la mesure par turbidimétrie des flux de matières en suspension dans les cours d'eau. *La Houille Blanche*(4), 50-56.

Thollet, F., Rousseau, C., Camenen, B., Boubkraoui, S., Branger, F., Lauters, F., & Némery, J. (2021). Long term high frequency sediment observatory in an alpine catchment: The Arc-Isère rivers, France. *Hydrological Processes, 35*(2), e14044. doi: 10.1002/hyp.14044

Torrent, J., & Barrón, V. (1993). Laboratory Measurement of Soil Color: Theory and Practice *Soil Color* (pp. 21-33).

Tramblay, Y., Ouarda, T. B. M. J., St-Hilaire, A., & Poulin, J. (2010). Regional estimation of extreme suspended sediment concentrations using watershed characteristics. *Journal of Hydrology, 380*(3), 305-317. doi: 10.1016/j.jhydrol.2009.11.006

Uber, M., Legout, C., Nord, G., Crouzet, C., Demory, F., & Poulenard, J. (2019). Comparing alternative tracing measurements and mixing models to fingerprint suspended sediment sources in a mesoscale Mediterranean catchment. *Journal of Soils and Sediments, 19*(9), 3255-3273. doi: 10.1007/s11368-019-02270-1

Valentin, C., Agus, F., Alamban, R., Boosaner, A., Bricquet, J. P., Chaplot, V., . . . Vadari, T. (2008). Runoff and sediment losses from 27 upland catchments in Southeast Asia: Impact of rapid land use changes and conservation practices. *Agriculture, Ecosystems & Environment, 128*(4), 225-238. doi: 10.1016/j.agee.2008.06.004

Vanmaercke, M., Poesen, J., Verstraeten, G., de Vente, J., & Ocakoglu, F. (2011). Sediment yield in Europe: Spatial patterns and scale dependency. *Geomorphology, 130*(3), 142-161. doi: 10.1016/j.geomorph.2011.03.010

Vauchel, P., Santini, W., Guyot, J. L., Moquet, J. S., Martinez, J. M., Espinoza, J. C., . . . Ronchail, J. (2017). A reassessment of the suspended sediment load in the Madeira River basin from the Andes of Peru and Bolivia to the Amazon River in Brazil, based on 10years of data from the HYBAM monitoring programme. *Journal of Hydrology, 553*, 35-48. doi: 10.1016/j.jhydrol.2017.07.018

Viville, D., Chabaux, F., Stille, P., Pierret, M. C., & Gangloff, S. (2012). Erosion and weathering fluxes in granitic basins: The example of the Strengbach catchment (Vosges massif, eastern France). *CATENA, 92*, 122-129. doi: 10.1016/j.catena.2011.12.007

Voichick, N., & Topping, D. J. (2014). Extending the turbidity record–making additional use of continuous data from turbidity, acoustic-Doppler, and laser diffraction instruments and suspended-sediment samples in the Colorado River in Grand Canyon. *US Geological Survey Scientific Investigations Report, 5097*, 31.

Voichick, N., Topping, D. J., & Griffiths, R. E. (2018). Technical note: False low turbidity readings from optical probes during high suspended-sediment concentrations. *Hydrol. Earth Syst. Sci., 22*(3), 1767-1773. doi: 10.5194/hess-22-1767-2018

1182 Vongvixay, A., Grimaldi, C., Dupas, R., Fovet, O., Birgand, F., Gilliet, N., & Gascuel-Odoux, C. (2018).
1183 Contrasting suspended sediment export in two small agricultural catchments: Cross-influence of
1184 hydrological behaviour and landscape degradation or stream bank management. *Land*
1185 *Degradation & Development, 29*(5), 1385-1396. doi: 10.1002/ldr.2940
1186 Walling, D. (1977). Limitations of the rating curve technique for estimating suspended sediment
1187 loads, with particular reference to British rivers. *Erosion and solid matter transport in inland*
1188 *waters, 122*, 34-78.
1189 Walling, D. E., & Fang, D. (2003). Recent trends in the suspended sediment loads of the world's rivers.
1190 *Global and Planetary Change, 39*(1–2), 111-126. doi: 10.1016/S0921-8181(03)00020-1
1191 Warrick, J. A., Madej, M. A., Goñi, M. A., & Wheatcroft, R. A. (2013). Trends in the suspended-
1192 sediment yields of coastal rivers of northern California, 1955–2010. *Journal of Hydrology, 489*,
1193 108-123. doi: 10.1016/j.jhydrol.2013.02.041
1194 Wass, P. D., & Leeks, G. J. L. (1999). Suspended sediment fluxes in the Humber catchment, UK.
1195 *Hydrological Processes, 13*(7), 935-953. doi: 10.1002/(SICI)1099-1085(199905)13:7<935::AID-
1196 HYP783>3.0.CO;2-L

Figure 1

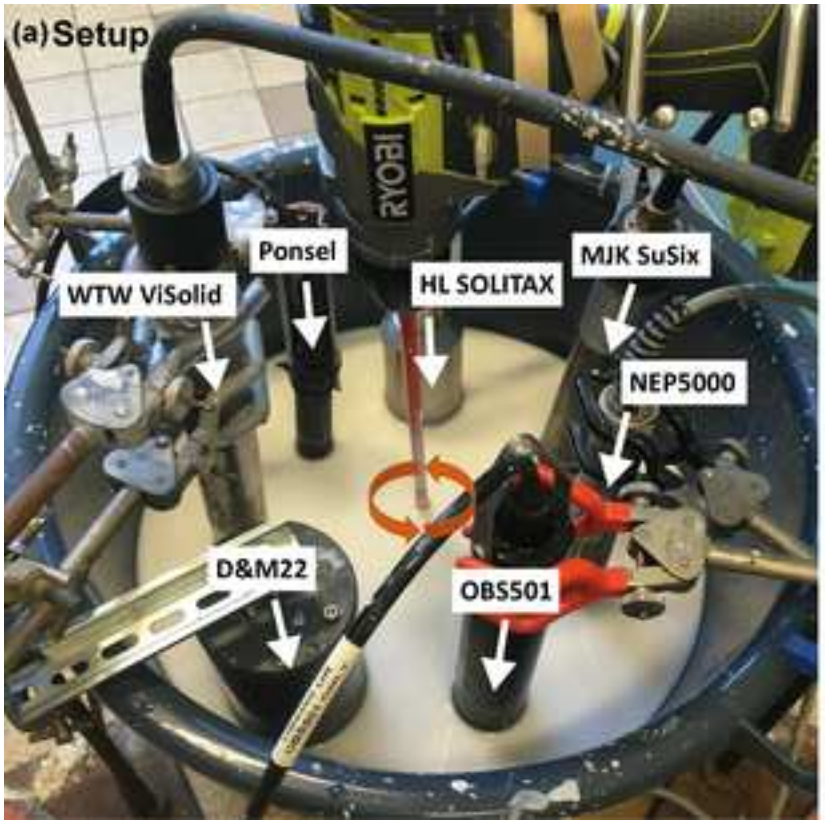

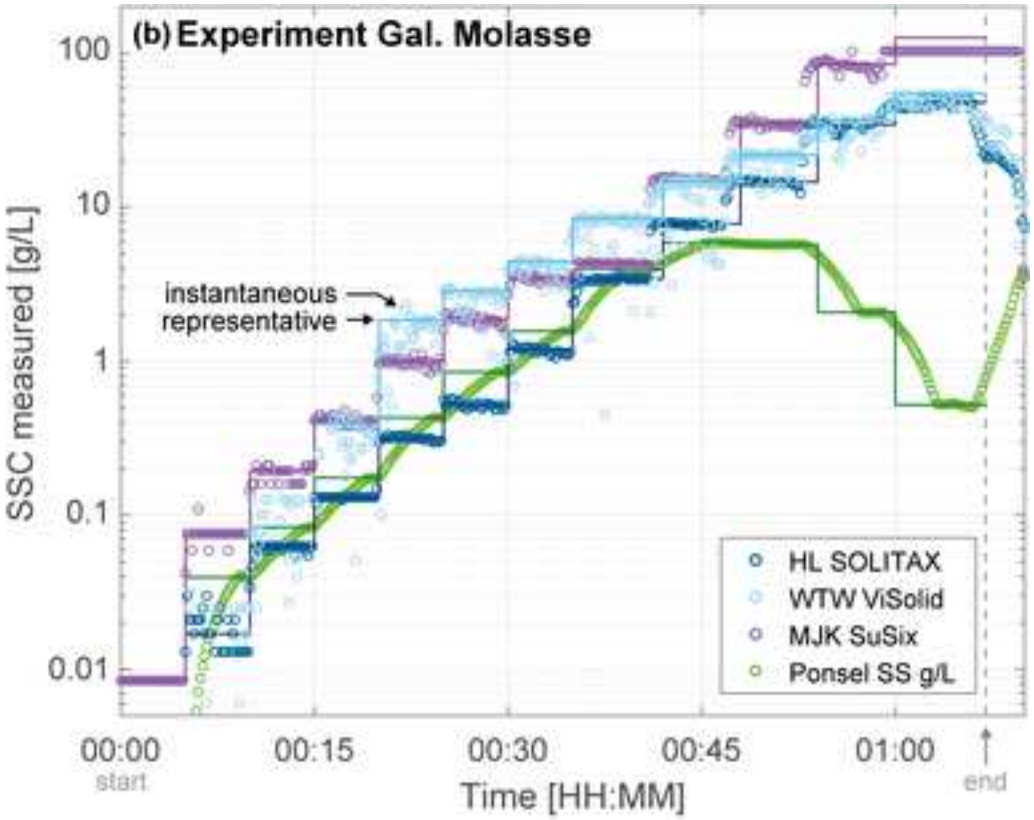

Figure 2

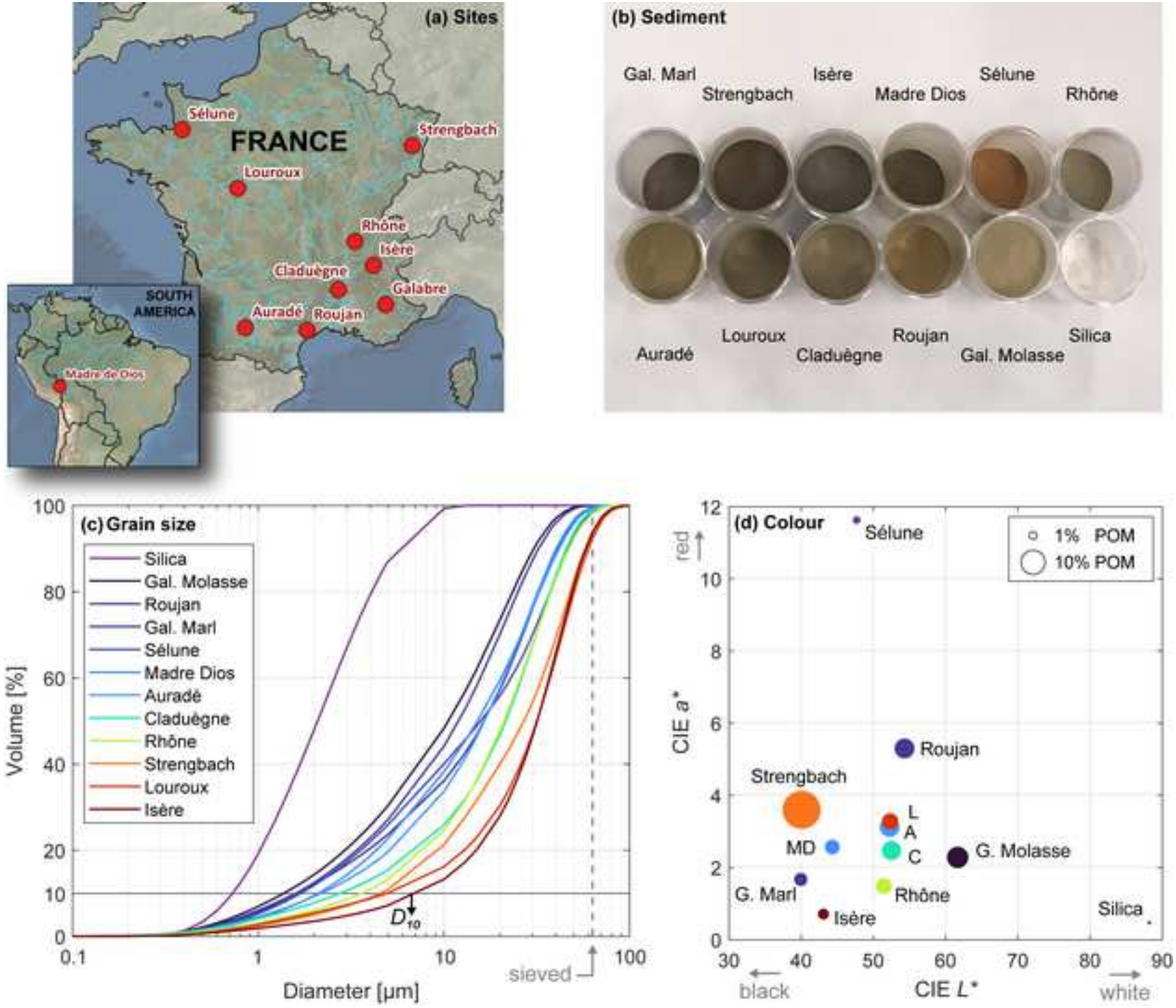

Figure 3

Click here to access/download;Figure - Upload high quality Images;Figure3.tif

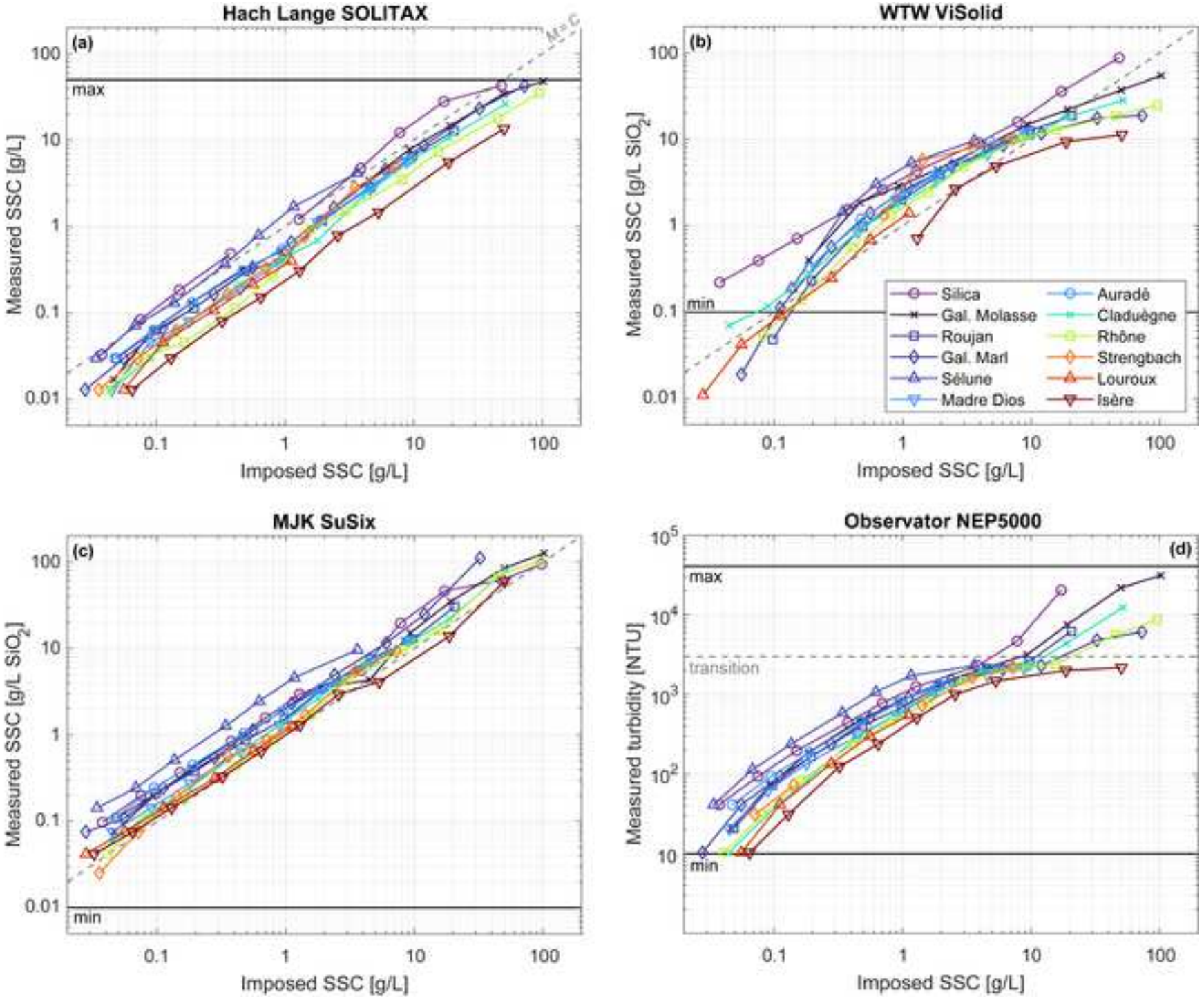

Figure 4

Click here to access/download;Figure - Upload high quality Images;Figure4.tif

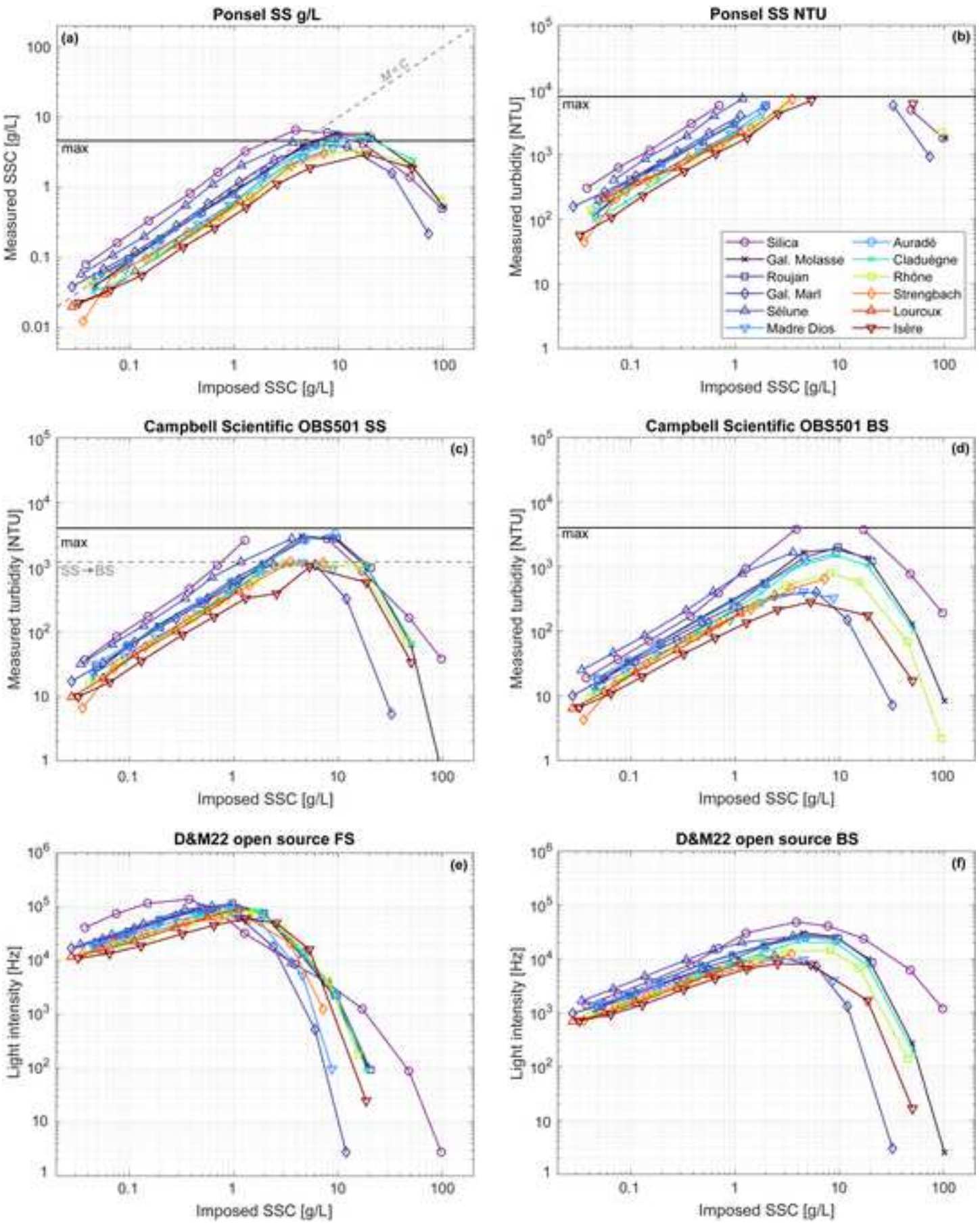

Figure 5

Click here to access/download;Figure - Upload high quality Images;Figure5.tif

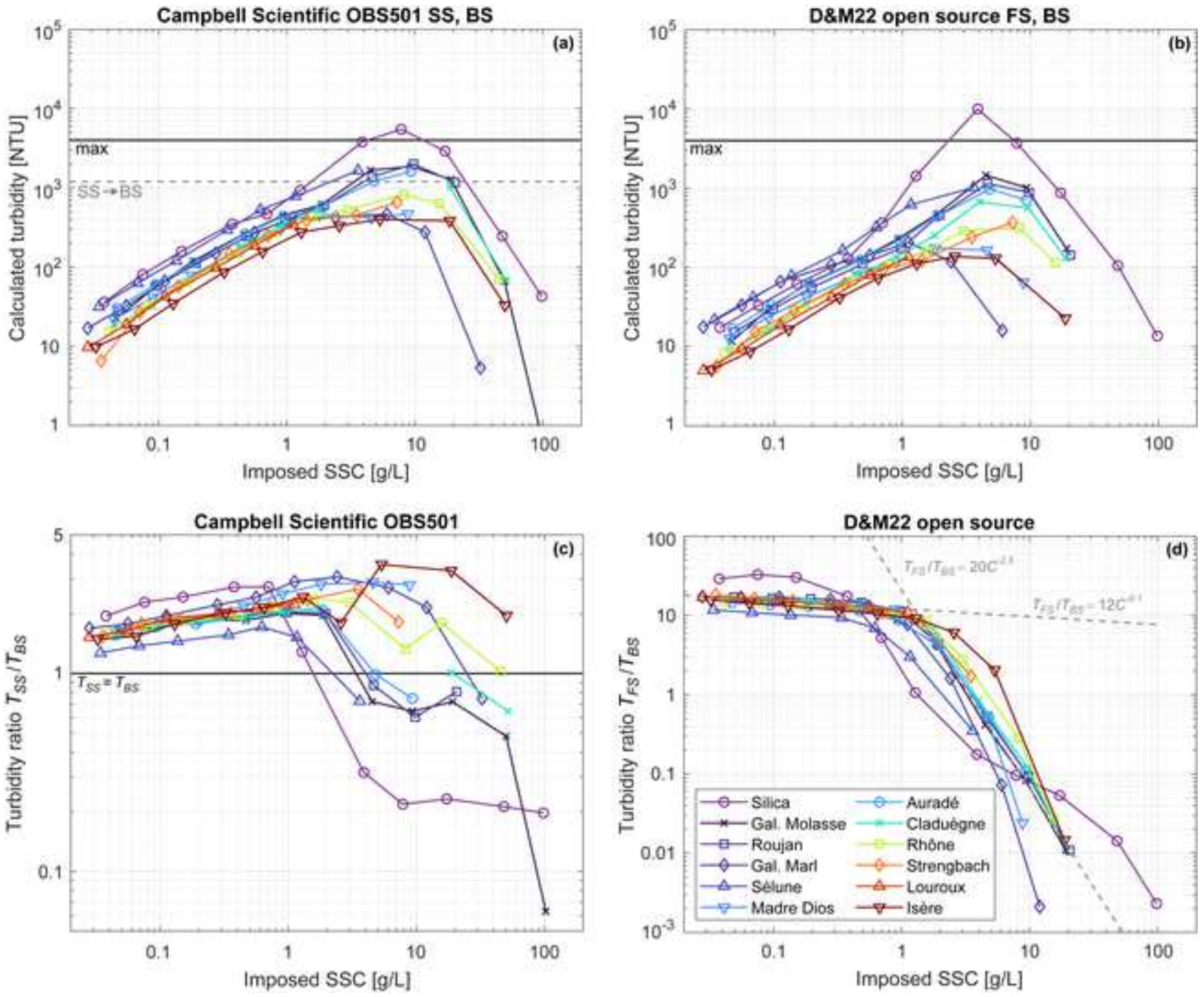

Figure 6

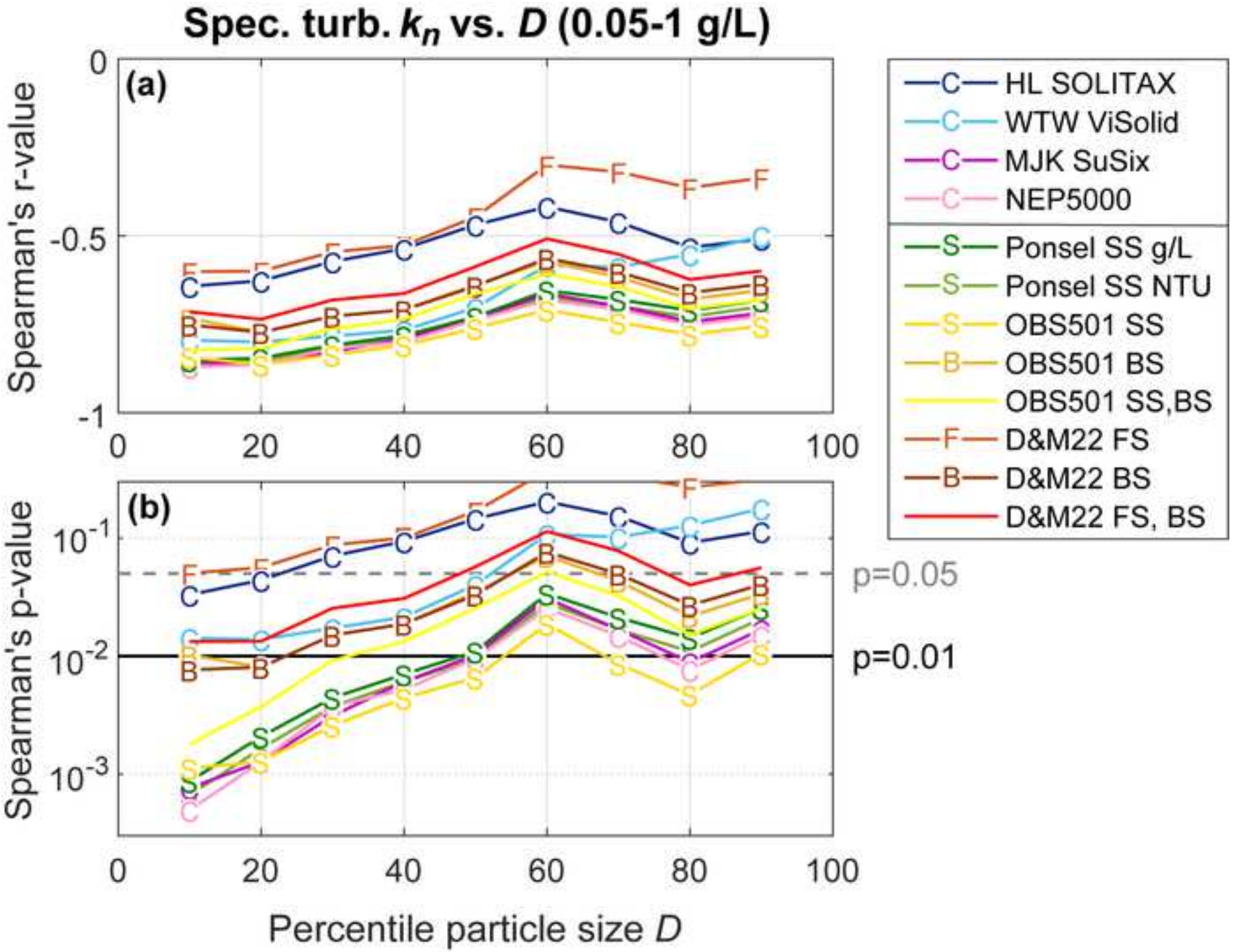

Figure 7

Click here to access/download;Figure - Upload high quality Images;Figure7.tif

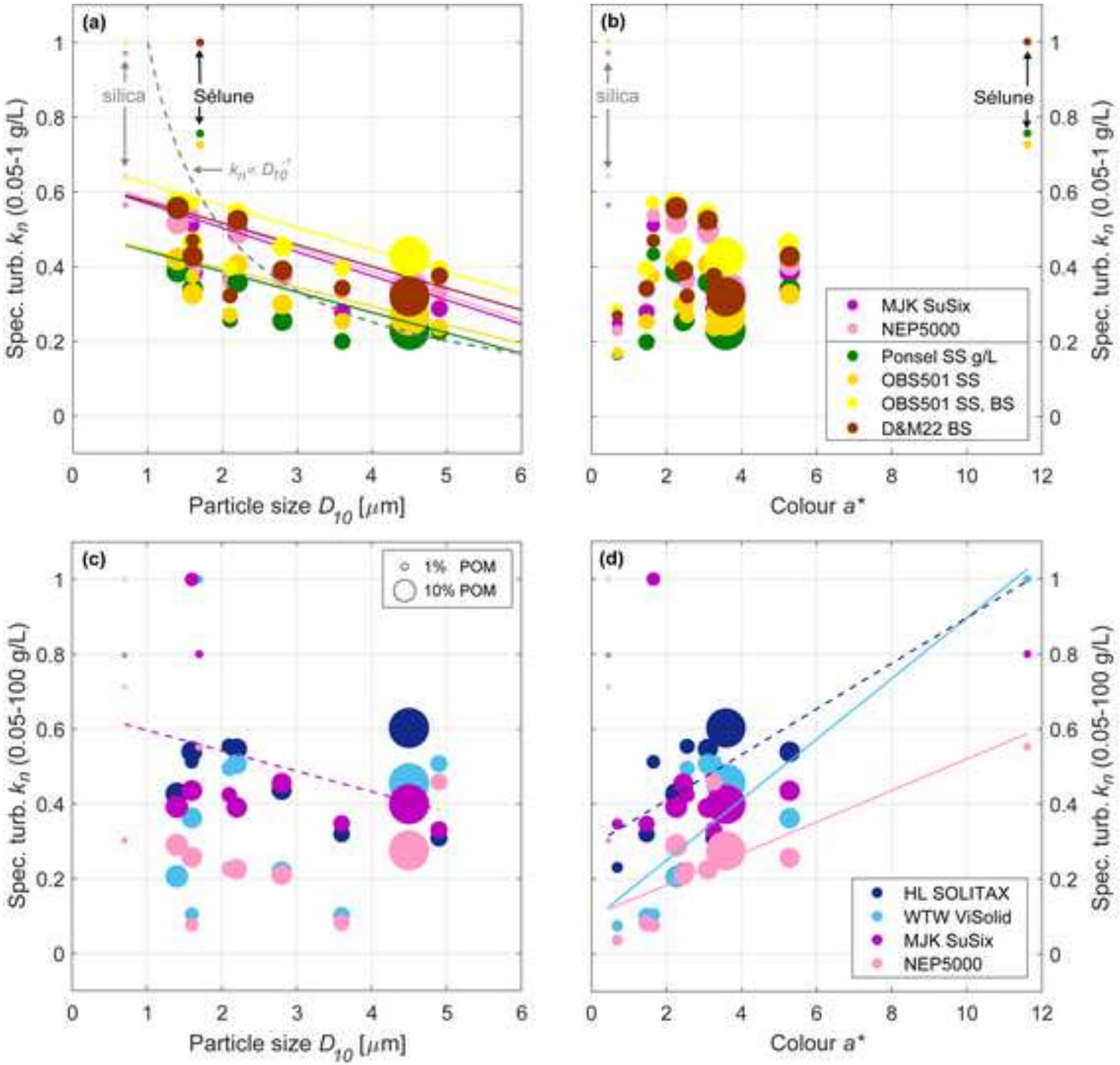

Figure 8

Click here to access/download;Figure - Upload high quality Images;Figure8.tif

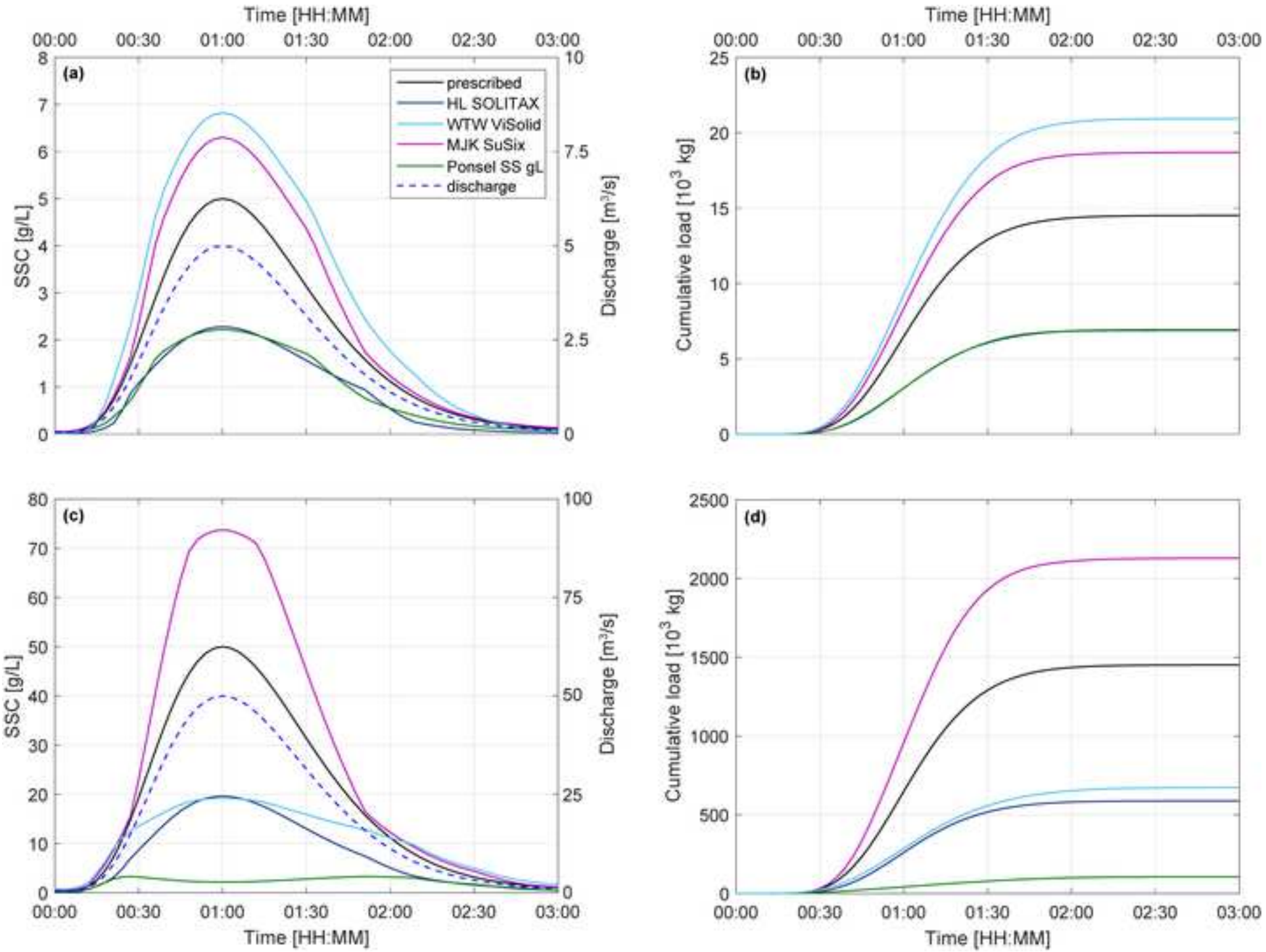

Figure A1

Click here to access/download;Figure - Upload high quality Images;FigureA1.tif

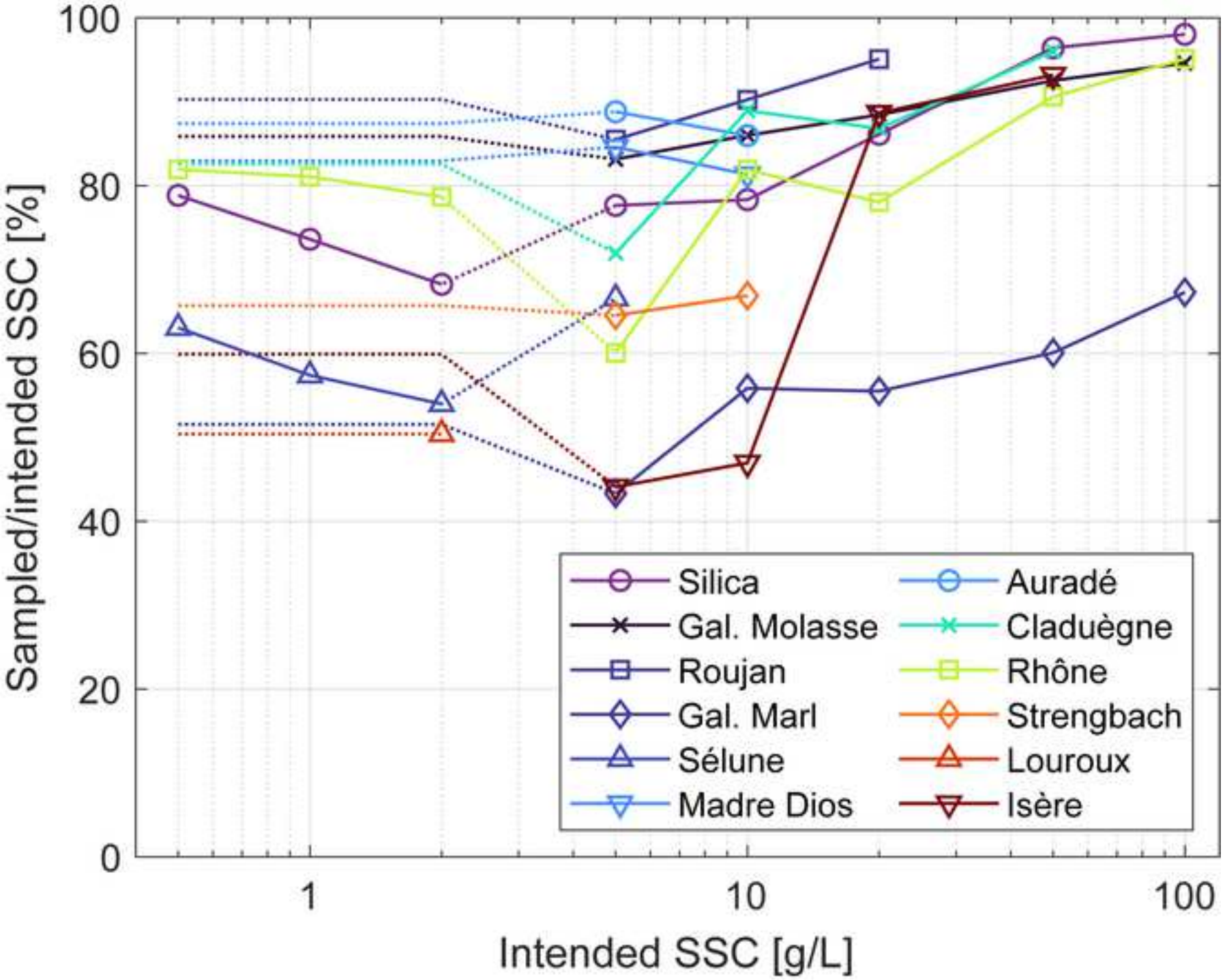

Figure 1: (a) Experimental setup with the seven investigated sensors placed around the mixer and a silica suspension in the water; (b) typical course of an experiment with the stepwise addition of sediment and instantaneous turbidity-based SSC measurements (10-second intervals) that were used to obtain representative values. Remarks: the sensors were not specifically calibrated directly prior to the experiments; WTW ViSolid, no stable measurements were obtained for concentrations <0.5 g/L; MJK SuSix, the analog measurements were limited to 100 g/L and the value >100 g/L was read from the transmitter display; Ponsel SS, the sensor requires ~4 minutes to establish a stable reading.

Figure 2: Sediment sources and characteristics; (a) river sites where sediment was obtained; (b) sieved sediment sorted per lightness L^* from top left to right bottom; (c) particle-size distribution of sediment sampled during the highest prescribed concentration of each experiment; (d) discriminating CIE colour parameters L^* and a^*, and POM content (point size) for the sediment sources; the colour scaling in (c) and (d) corresponds to D_{10}.

Figure 3: (d) Turbidity and (a, b, c) turbidity-based measurements of combined-signal sensors versus imposed SSC. The colour scaling of sediment sources corresponds to particle size D_{10} (see Figure 2c). A $M = C$ relationship (a, b, c) and an apparent transition in the turbidity vs. SSC (d) are indicated. Manufacturer-prescribed minimum and maximum values are provided (if they fall within the displayed measurement range).

Figure 4: Turbidity and turbidity-based measurements of individual-signal sensors versus imposed SSC. The colour scaling of sediment sources corresponds to particle size D_{10} (see Figure 2c). A $M = C$ relationship is indicated (a). Manufacturer-prescribed minimum and maximum values are provided (if they fall within the displayed measurement range) and the prescribed transition from OBS501 SS to BS (c) is indicated.

Figure 5: (a, b) Calculated turbidity based on multiple signals and functions provided by the manufacturer/developer (see section 2.1) versus imposed SSC. (c, d) Turbidity ratios (dimensionless) versus imposed SSC. The prescribed transition value from OBS501 SS to BS (a) and the transition from $T_{SS}>T_{BS}$ to $T_{SS}<T_{BS}$ (c) are indicated.

Figure 6: Spearman's rank correlation (a) r-value and (b) p-value of normalized specific turbidity k_n per sensor and signal as a function of particle size percentile.

Figure 7: Normalized specific turbidity k_n per sensor and signal as a function of (a, c) particle size D_{10} and (b, d) CIE colour a^* for the concentration ranges of 0.05–1 g/L and 0.05–100 g/L. POM content is shown as point size (see Figure 2d). Solid regression lines are significant (p<0.01), dashed lines are marginally significant (p<0.05) and a grey dashed curve with $k_n \propto D_{10}^{-1}$ is added for reference. In (a), we only included sensors with p<0.01 which are also shown in (b); we omitted Ponsel SS NTU, which only marginally differs from Ponsel SS g/L, for visibility purposes. All correlation parameters are provided in Table C1.

Figure 8: Sensor-dependent differences in (a, c) SSC and (b, d) cumulative sediment load for two fictive flow events with Rhône sediment. Note that the sensors were not specifically calibrated for this purpose and that the deviation from the prescribed concentration is not an indication for sensor performance.

Figure A1: Relative amount of sampled SSC per intended SSC and sediment source. The colour scaling corresponds to particle size D_{10} (see Figure 2c).